ACTIVE TURBULENCE GENERATION IN A 3/4 OPEN-JET WIND TUNNEL

JOSHUA MARQUES

A THESIS SUBMITTED TO THE FACULTY OF GRADUATE STUDIES
IN PARTIAL FULFILMENT OF THE REQUIREMENTS
FOR THE DEGREE OF

MASTER OF APPLIED SCIENCE

GRADUATE PROGRAM IN MECHANICAL ENGINEERING
YORK UNIVERSITY
TORONTO, ONTARIO
DECEMBER 2022

Abstract

The focus of this thesis is on the replication of on-road turbulent flow conditions within a 1/10th scale model of a 3/4 open-jet closed-loop return wind tunnel. This type of wind tunnel is commonly used in the automotive industry for testing aerodynamic performance of vehicles. Often, these types of wind tunnels are used to produce a clean laminar flow and testing results are limited to these idealized conditions. A novel system is designed to produce a wide range of turbulence scales in the scale model automotive wind tunnel using activated grid elements. It is shown that the turbulence produced by the novel turbulence generation system can generate turbulent flows having Taylor Reynolds numbers between 70 and 890, and turbulence intensities between 3.3 % and 33.1 %, depending on proximity to the grid.

Table of Contents

List of Tables

List of Figures

Symbols & Acronyms

Roman

C_ϵ = Dissipation rate constant

$E(f)$ = Energy spectrum in the streamwise direction based on the frequency

$E(\kappa)$ = Energy spectrum based on the wave number

f = Frequency (Hz)

f_r = Reduced frequency

I = Anisotropy ratio

L_c = Characteristic length (m)

L_u = Longitudinal integral length scale (m)

L_v = Spanwise integral length scale (m)

L_w = Vertical integral length scale (m)

M = Mesh size (m)

q = Turbulent kinetic energy (m^2/s^2)

Re_λ = Reynolds number based on the Taylor microscale

Re_M = Reynolds number based on the mesh length of the grid

Ro = Rossby number

TI_u = Longitudinal turbulence intensity (%)

TI_v = Spanwise turbulence intensity (%)

TI_w = Vertical turbulence intensity (%)

TI_q = Turbulence intensity based on the turbulent kinetic energy (%)

u = Velocity fluctuations about the mean velocity (m/s)

U = Mean free stream velocity (m/s)

v = Kinematic viscosity (m^2/s)

$*' = '$ denotes a RMS quantity where $*$ is a statistical variable

$\langle * \rangle = \langle * \rangle$ denotes an ensemble average

Greek

ϵ = Dissipation rate ($\mathrm{m}^2/\mathrm{s}^3$)

κ = Wave number (m^{-1})

λ = Taylor microscale (m)

τ = Integral time scale

Ω = Mean rotational rate (Hz)

Acronyms

AoA = Angle of attack

HIT = Homogenous isotropic turbulence

NRC = National Research Council of Canada

TGS = Turbulence generation system

1 Introduction

The aerodynamic testing of vehicles in a wind tunnel is an integral step of the design process to optimize the performance of a vehicle. Most automotive wind tunnels are designed to simulate a vehicle travelling along a road in undisturbed air. Turntables are often fitted to the floor of the wind tunnel to rotate the vehicle to simulate a crosswind. However, on-road flow conditions are often much more complex than that previously described. The flow conditions experienced by vehicles on the road vary depending on, for example, proximity to other vehicles [1], the topology of the region and other roadside obstacles [1], and the atmospheric boundary layer [2]. The discrepancy between on-road conditions, the idealized testing conditions in automotive wind tunnels, and observed differences in measured or simulated performance [1–7] of vehicles have created demand for controlled wind tunnel-based testing with more realistic flows.

A system designed to produce turbulence in a wind tunnel is referred to herein as a turbulence generation system (TGS). Several TGSs have been used to model

on-road turbulence conditions in wind tunnels with varying degrees of success [8–12]. The aforementioned past systems used to generate turbulent flows in wind tunnels can sub-classified as either passive or active. Passive systems use static bluff bodies placed upstream of the testing section to generate unsteady wakes. A common example of this type of system would include a grid of square bars installed in the settling chamber of the wind tunnel. Active systems use motion to steer the flow or to dynamically vary the blockage of the flow upstream of the testing section. Examples of active systems include oscillating airfoils, designed to steer the flow, or rotating bars placed upstream of the test section to vary the blockage.

While passive systems can input turbulence in the testing section, the resulting turbulence tends to be not well represented over the full range of the corresponding scales measured on the road [7]. Specifically it is the long length scales or low frequency fluctuations that passive systems are unable to produce, which represent an important range in the spectrum flows observed on-road [7, 8, 13, 14]. Mydlarski [15] states that passive systems tend to produce length scales on the order of L_u/M <1 while active systems produce length scales on the order of L_u/M >1 where L_u is the integral length scale, defined as the size of the largest energy containing eddies in a turbulent flow, and M is the mesh length. In an active grid system, the mesh length is the distance between two adjacent shafts as seen in the left figure of Figure 1.1 while in a passive system, the mesh length refers to

the on-center distance between adjacent grid bars, as shown in the right figure of Figure 1.1.

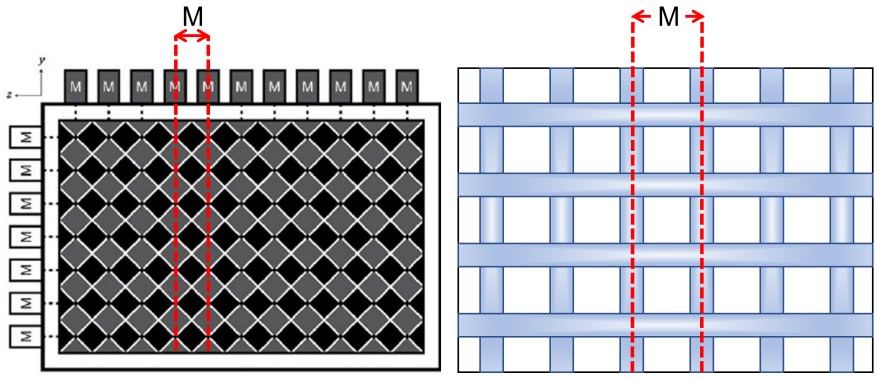

Figure 1.1: An active grid (reprinted with permission) [16] (left) and an passive grid schematic (right) showing the definition of a mesh length (M) for each type of system.

Compared to passive grids, active grids are a relatively newer technology, having only been in use for a few decades. Active grids are more capable with respect to the range of turbulence they can produce, with the potential to tailor the range of turbulence characteristics through different blockages, forcing protocols, and initial conditions [16].

The motivation for the present thesis is to recreate on-road turbulence conditions in an automotive wind tunnel. This thesis concerns development and characterization of the turbulent flow created by an active TGS. The novel TGS described in this thesis is comprised of three subsystems. The first, and focus of this thesis, is an active grid to generate broad band turbulence. The second subsystem is designed

to produce unsteady streamwise flow, such as gusts, and the third subsystem is designed to produce time varying yaw. The results pertaining to the active grid portion of the novel TGS system are considered in this thesis, and are the main contribution. Since the active grid was designed to work in parallel and accommodate the other subsystems, reference to them or their effects on the results, are found in this thesis.

The first objective of this thesis was to design the physical active grid subcomponent of the novel TGS having active yaw and unsteady flow capability. The objective of the active grid is to reproduce on-road turbulent flow characteristics already reported in the literature within a 1/10th scale model 3/4 open-jet automotive wind tunnel. The second objective is to quantify how active grid inputs, such as non-dimensional rotational rates, effect the range turbulence levels created or the distribution of the spectrum (a measure of the distribution of turbulence scales), and compare these with desired target conditions. Based on the results of the work, recommendations on choice of operating protocols and system design parameters will be made.

2 Literature Review and Related Theory

This thesis concerns the development of a system to be employed in a model-scale 3/4 open-jet wind tunnel to simulate on-road flow conditions. Three main sections follow, the discussion of literature concerning on-road flow conditions, active and passive turbulence generation technology, and review of existing full scale automotive wind tunnel systems designed to simulate aspects of on-road flow conditions.

2.1 Turbulence

Turbulence is described as the irregular or random movement of fluid particles in both the time and space domains caused by fluctuating pressure gradients in the flow [17]. One common type of turbulence is referred to as homogeneous isotropic turbulence (HIT). For homogeneous isotropic turbulence the statistics of the turbulence are the same throughout space and are the same in every direction.

The instantaneous streamwise velocity of a fluid can be expressed as $U + u$,

where U is the mean of the velocity and u is the velocity fluctuations about the mean. Other components of the flow such as the lateral and vertical components can similarly be expressed as $V + v$ and $W + w$ respectively. The investigation of turbulence is generally centered around the velocity fluctuations and can be expressed in terms of its intensity, length scale, and its energy distribution spectra. The turbulence intensity, $u' = \langle u^2 \rangle^{1/2}$, is a measure of the level of flow fluctuations divided by a reference value, usually the mean velocity: $TI_u = u'/U$. The other turbulence intensity components in the spanwise and vertial directions are similarly expressed as $TI_v = v'/U$ and $TI_w = w'/U$ respectively. Turbulence intensity can also be expressed in terms of turbulent kinetic energy by $TI_q = \langle q^2 \rangle^{1/2}/\sqrt{3}U$ where $q^2 = u'^2 + 2v'^2$ which assumes that v'^2 is approximately equal to w'^2 [18]. For the quantities presented herein, the former method is used unless otherwise stated.

The integral length scale (L_u) is defined as the size of the largest energy containing eddies in a turbulent flow. One of the most common methods employed by researchers to calculate the integral length scale of a turbulent flow is by taking the autocorrelation of the velocity fluctuations signal. The autocorrelation coefficient function, given below, indicates the time over which a signal is correlated with itself [19].

$$\rho(t_*) = \frac{\langle u(t)u(t+t_*) \rangle}{\langle u^2 \rangle}$$

Integrating the autocorrelation coefficient functions to its first zero crossing (t_0) yields the integral time scale (τ) which can be converted to a length scale by

employing Taylor's frozen-field hypothesis by $L_u = \tau U$ [19].

$$\tau = \int_0^{t_0} \frac{\langle u(t)u(t+t_*)\rangle}{\langle u^2\rangle}\, dt_*$$

Similarly, the integral time scales (τ) and subsequently the integral length scales of the spanwise (L_v) and vertical (L_w) components can also be calculated in the same way.

Perhaps even more useful in comparing turbulent flows is to compare the energy spectra $E(\kappa)$, where κ is the wave number. The energy spectra is a measure of the the turbulent kinetic energy (TKE) in the frequency domain $E(f)$, or in the context of this thesis, in the wave number domain, $E(\kappa)$. The energy spectra is calculated by taking the Fast Fourier Transform of the velocity signal. The wave number is derived from the frequency by: $\kappa = 2\pi f/U$. An example of the typical shape of the energy spectrum is shown in Figure 2.1. The left-most region of the spectra, shown by the green arrow, depicts the energy containing region where scales are known as the integral scales. After the energy containing region is the inertial subrange where the turbulence decays with a -5/3 power law. Scales in this inertial subrange region are known as the Taylor microscale. The final region, the dissipation region, is where viscous forces dissipate the remaining turbulence as heat. Scales in this region are known as the Kolmogorov scales.

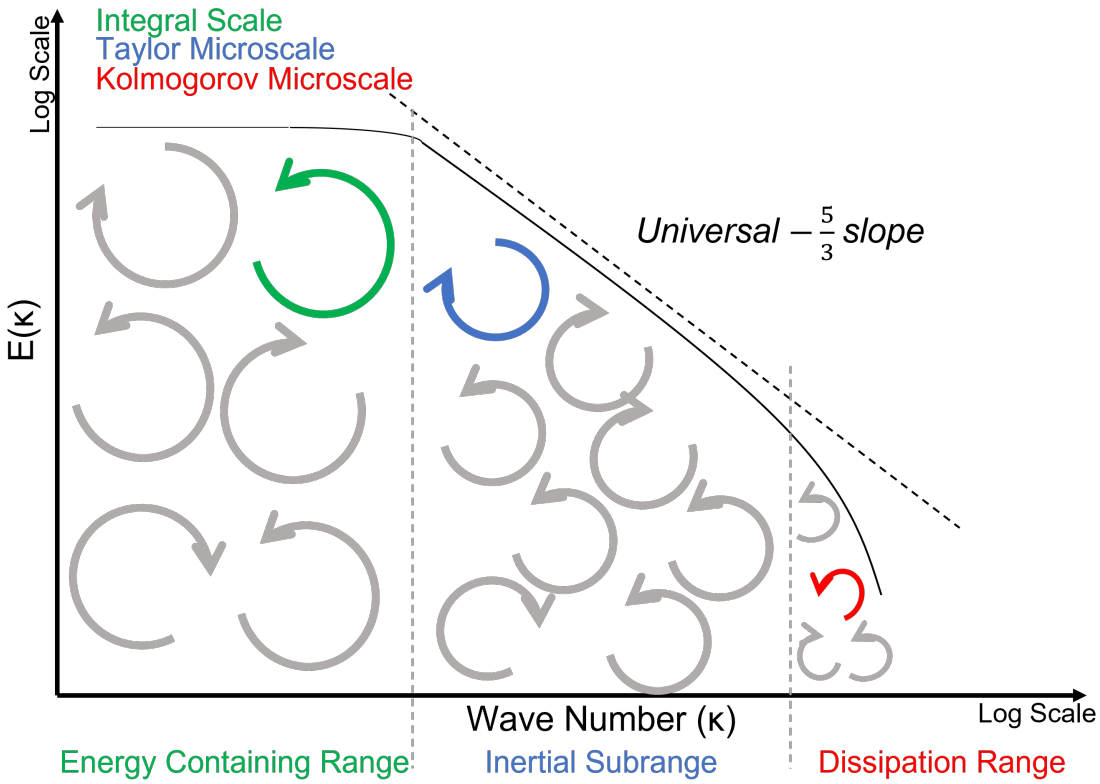

Figure 2.1: The energy cascade highlighting the integral scales, inertial subrange, and the dissipation range.

On-road measurements by Gordon et al. [20, 21] show that the presence of other vehicles on highways greatly increase the energy spectral density of the TKE when compared to driving isolated from other traffic. Rao et al. [22] shows that the high frequency (>0.5 Hz) end of the on-road spectra is enhanced in the wake of a vehicle travelling on the road. In addition, the presence of a strong headwind coupled with the presence of traffic can produce intense shear that results in large eddies forming [23].

2.2 Road Conditions

A survey of the available literature [1–5, 13, 14, 24–26] established the goals for the turbulent flow conditions that are typically experienced by vehicles and to support a defined target for the turbulence conditions to be recreated in the $1/10^{th}$ model scale wind tunnel. The characteristics of the on-road environment or conditions are an important factor to consider when discussing on-road flow measurement results from various sources in the literature. For example, flow conditions vary depending on the terrain in proximity to the road [1–3, 5, 13, 14]. Common terrains tested include smooth open roads, roads with obstacles located near the sides, and highways with effects of traffic [1, 3, 14]. The presence of other vehicles (and the traffic density) will affect the airflow passing over the test vehicle [1, 3, 4]. Metrics that were considered in this literature review were:

- Turbulence length scale - defined as the size of the large energy containing eddies or vortices in a turbulent flow.
- Turbulence intensity - a measure of the level of flow fluctuations divided by a reference flow velocity.
- Turbulence energy spectrum - distribution of the flow fluctuations with frequency.
- Yaw angle - the actual oncoming flow angle experienced by a vehicle.

The relevant data were collected and sorted according to the terrain, traffic, and wind conditions present during the time of the testing. The most common

conditions were categorized into three main ranges as shown in Table 2.1. The aim for this system is to be able to recreate all of the ranges listed below - low, medium, and high. The low range case consists of open roads without traffic, wind, or roadside obstacles (RSO). The medium range case encompasses the low range case with the addition of roadside obstacles and highway (HW) terrains that include some traffic, wind, and vegetation at the roadside. The medium range case is the case that is most commonly found on-road [1]. The high range case encompasses overtaking manoeuvres as well as trailing behind a heavy-duty transport truck.

Range	TI_u (%)	TI_v (%)	TI_w (%)	L_u **(m)**	L_v **(m)**	L_w **(m)**	**Comments**
Low	4	4	2	5	5	0.5	Smooth open roads with light traffic/wind
Medium	6	6	4	2.5	2.5	0.5	Low spec. + RSO/HW terrains with moderate traffic/wind
High	9	9	7	1	1	0.5	Medium spec. + trailing/overtaking manoeuvres with heavy traffic

Table 2.1: Summary of turbulence intensity and length scales for different terrain and traffic conditions. Data averaged from [1–5, 13, 14, 24–26].

Wordley and Saunders [14] suggest rather than comparing flows based on intensity and length scale, it is perhaps more straight forward to consider comparisons of the

energy spectra. Sims-Williams [7] explains that turbulent flows can be described as being quasi-steady when the reduced frequency, $f_r = (2\pi L_c)/L_u$, where L_c is the characteristic length of the vehicle, and L_u is the integral length scale, is less than 0.1 and not quasi-steady when the reduced frequency is greater than 1. This is to say that if $L_c = 4$ m and the vehicle was travelling at 30 m/s, then the vehicle would traverse through each large turbulent structure every ≈ 0.8 s for $f_r = 1$ and $L_u = 25$ m, and ≈ 8 s for $f_r = 0.1$ and $L_u = 250$ m. For quasi-steady flow, for example, the measured drag or lift would be the same as that determined for a direct average of the range of the flow events occurring. Figure 2.2 illustrates the envelope of the range of on-road spectra with the associated frequency, time scale, length scale, length scale normalized by the vehicle length (λ/L), and the reduced frequency.

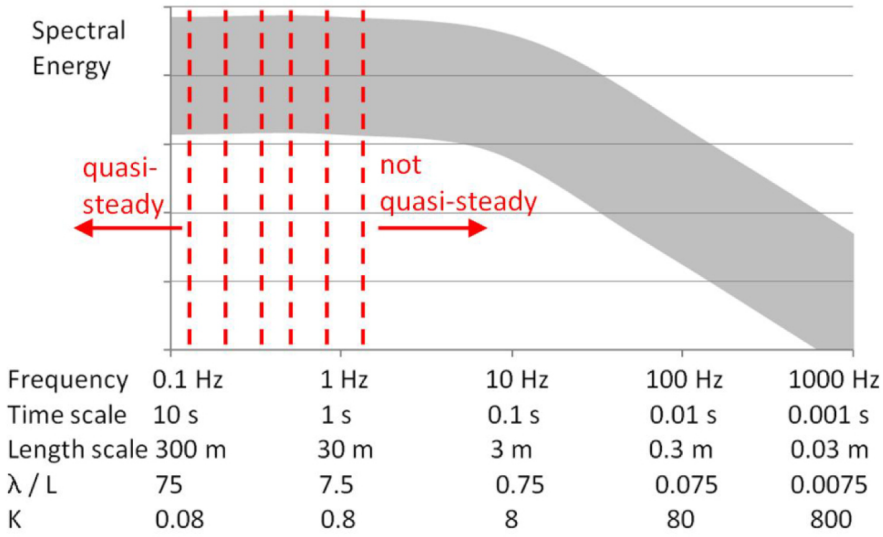

Figure 2.2: The spectral energy envelope as measured on-road with the corresponding frequency, time scale, turbulence length scale, and reduced frequency where $U_{ref} = 30$ m/s [7]. Reprinted with permission.

2.3 Existing Full Scale Turbulence Generation Technologies

There are several full-scale automotive wind tunnels in operation that have systems designed to simulate on road flow conditions. These systems are summarized in Table 2.2. The most common types of TGSs utilize static rectangular bars [27, 28] or oscillating airfoils placed at the nozzle [9, 10, 12, 29, 30]. However, a recent active yaw system was designed using airfoils with an active flap [28]. It will be referred to herein as the FKFS Active Flaps system. This type of system can be desirable as the lower inertia of the flap allows the system to reach higher oscillation frequencies. Notably, the active systems consistently produce greater turbulence

intensity and length scales than the passive systems. The counter example is the National Research Council of Canada's (NRC) passive system, shown in Table 2.2. The NRC passive system [27] produced higher length scales than most of the active systems due to the passive grid elements being placed upstream of the contraction. By doing this, the longitudinal length scales are stretched by the contraction with the negative side effect of reducing the lateral turbulence intensity and length scale.

Three examples of turbulence generation systems can be seen in Figure 2.3. The image on the left is the TGS in the Pininfarina tunnel [11]. The system uses 5 vortex generators to produce turbulence. Each vortex generator can be made to widen and narrow by active oscillation about the vertical axis that the wings of the vortex generator are attached to. The middle image is Toyota's Natural Wind Generator system [10] in their automotive wind tunnel utilizing an airfoil system to dynamically yaw the flow. Shutters along the top of the nozzle that can open and close to add and remove blockage in order to give the effect of gusting. The image on the right is the FKFS Flaps system [28] which uses stationary airfoils with a movable flap to yaw the flow. In addition, the system incorporates a passive system consisting of flat vertical bars to induce high frequency vortex shedding.

Facility	TI_u (%)	L_u (m)	Yaw (°)	Freq. (Hz)	Class	Description
NRC [27]	4.4	2.6	-	-	Passive	6 V-Shaped spires upstream of contraction
Pininfarina [11]	7.1	-	6	-	Active	5 vortex generators at the opening
Durham [12]	10.0	-	11	10	Active	Airfoil-Shutter system across entire test section.
Toyota NWG [10]	13.0	1.8	12	5	Active	Airfoil cascade and damper system
FKFS Swing [9]	4.5	0.9	-	5/10	Active	8 independently controlled airfoil cascade
FKFS Flaps [28]	5.6	2.5	6.5	50	Hybrid	Airfoils with active flaps and passive bars

Table 2.2: Specification summary of turbulence generation systems used in automotive wind tunnels. The maximum values of the turbulent intensity, length scale, yaw angle and operation frequency (if applicable or known) is shown as well as the class denoted as passive, active or hybrid.

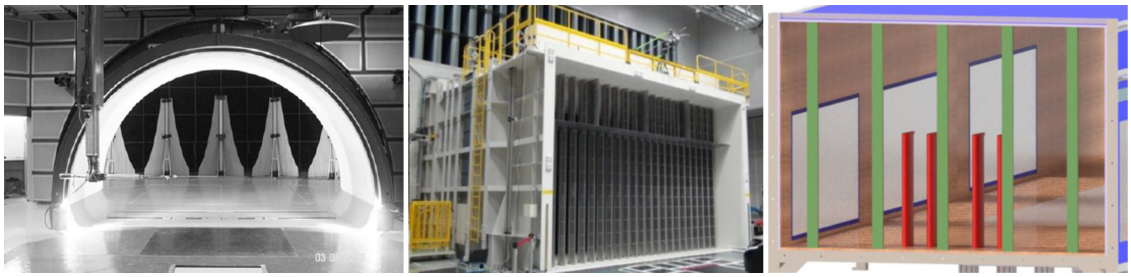

Figure 2.3: Pininfarina active drag-based TGS (left) [11], Toyota active lift-based TGS with shutter system (middle) [10], FKFS Active Flaps lift-based TGS with passive bars (right) [28]. Reprinted with permissions.

Efforts to recreate on-road turbulent flow conditions in full scale wind tunnel tests have been met with some success. A common method to compare results from

different facilities is using the energy spectra plotted against the reduced frequency as was shown previously in Figure 2.2. In Figure 2.4, the corresponding spectra from three different wind tunnel facilities [11, 27, 31, 32], are plotted with example data measured on-road by [1] using multi-hole probes. The reduced frequency, given as $f_r = (fL_{ref})/(U_{ref})$, is used to compare the normalized spectra for different mean velocities and scale. L_{ref} is taken as the reference length, normally 1 m, while U_{ref} is the reference velocity taken as the speed of the vehicle for on-road measurements or the velocity of the wind in a wind tunnel. In Figure 2.4, the dashed lines are the measured turbulence spectra for roadways under different traffic conditions [1] while the coloured lines are the measured spectra from some different automotive turbulence generation systems. The dark blue line shows the turbulence spectra from a typical wind tunnel without any additional turbulence generation system. The yellow line is a turbulence system that consists of a net that is allowed to vibrate in the flow [32]. The *turbulence net* is able to recreate a range of high frequency turbulent flow that corresponds with the similar turbulent flow measured on road but does not noticeably improve the low frequency components compared to the empty wind tunnel. The turbulence produced by the *passive spires* [33] is shown by the cyan line. The spires are shown to greatly improve the mid to high frequency components of the flow but again are unable to reproduce the low frequency components found on-road. Lastly, the purple line depicts the Pininfarina

active drag-based hybrid system [11], also shown in the left figure of Figure 2.3. The Pininfarina system uses flapping spires to produce turbulence, where the flapping motion is used to generate additional low frequency components. The system produces a spectra that mimics the low frequency components of on-road turbulence quite well; however it provides too much energy at the higher frequencies.

None of the systems presented in Figure 2.4 can reproduce the on-road spectra perfectly. They either overshoot in the high frequencies, like the Pininfarina system, or they undershoot at the low frequencies, like the *Narrow Spires, RTS,* and *Turbulence Net.*

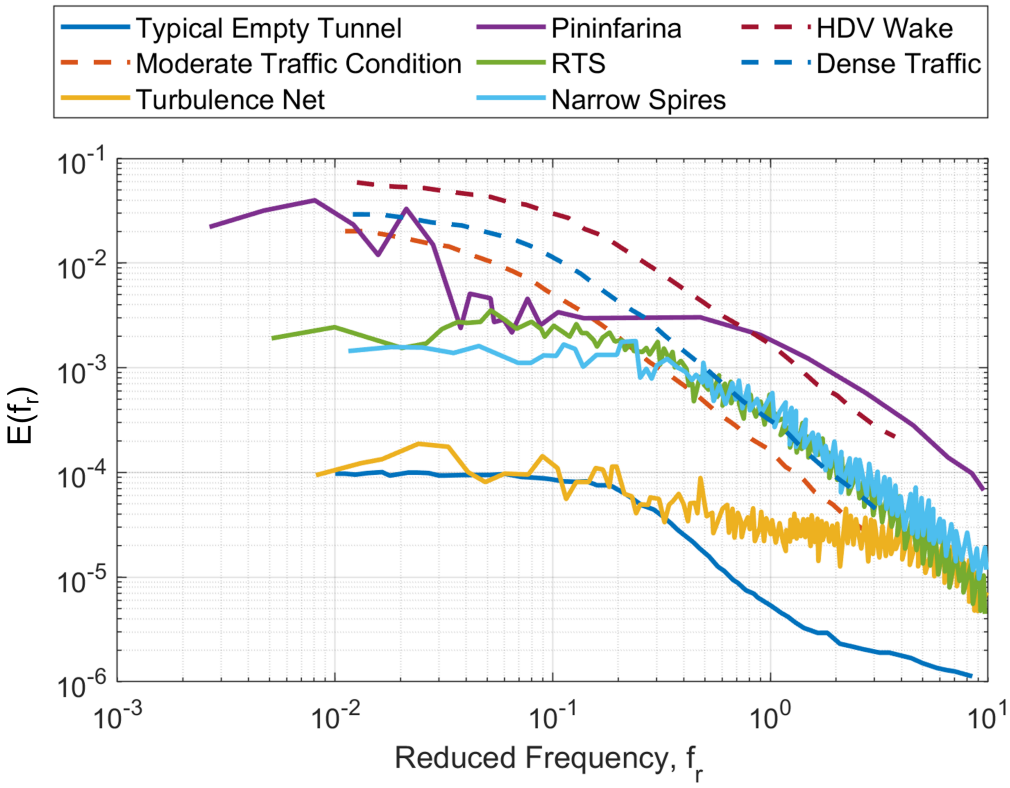

Figure 2.4: Turbulence spectra reproduced from the data given in [8] for various turbulence generation systems plotted against the measured on-road spectra.

2.4 Passive and Active Methods of Turbulence Generation

Turbulence in a wind tunnel can be created by means of a passive system or an active system. A passive system utilizes horizontal bars, vertical bars, or a combination of both placed upstream of the contraction to produce turbulence through the natural vortex shedding from the blunt object in the flow. Passive systems, an example of

which can be seen in Figure 2.5, characteristically produce low turbulence intensities and small length scales at the location in the wind tunnel where the turbulence would be considered homogeneous and isotropic [34]. In addition, passive systems are unable to inject sufficient low-frequency energy into the flow required to achieve a sufficiently high local Reynolds number. The local Reynolds number, given by $\mathrm{Re}_\lambda = u'\lambda_g/v$, is the Reynolds number based on the Taylor microscale λ_g, referred to herein as the Taylor Reynolds number or local Reynolds number. The Taylor microscale, given by $\lambda_g = \sqrt{15vu'^2/\epsilon}$ [35], is a representation of the largest scales in the dissipative range [36] and is based on u' and the dissipation rate, ϵ, given by $\epsilon = 15v\overline{(\partial u/\partial x)^2}$. Scales smaller than this are significantly affected by fluid viscosity and are dissipated as heat. The Taylor Reynolds number is a representation of the influence of the inertial subrange on the flow. Generally, flows with a larger Re_λ will show characteristics that match Kolmogorov's predicted universal turbulence characteristics [19]. A Flow with a sufficiently high Re_λ will tend to have a well developed inertial subrange in the energy spectra. Passive grids rarely exceed a Taylor Reynolds number of $\mathrm{Re}_\lambda = 100 - 200$ [16, 37] while the accepted minimum local Reynolds number to be able to view the -5/3 slope in the inertial subrange of the spectrum is $\mathrm{Re}_\lambda < 250$ [37]. To increase this local Reynolds number, an active system is required.

Figure 2.5: Passive vertical spires placed in the settling chamber of the National Research Council of Canada's 9 m wind tunnel [27]. Reprinted with permission.

An active system uses motion to dynamically vary the blockage of the flow in order to increase the turbulence intensity, length scale, and local Reynolds number of the flow by means of oscillating [38], rotating [37], or vibrating objects [39, 40] placed upstream of the test section. Some examples of active systems include the Pininfarina [11] drag-based turbulence generation system which uses tall flapping spires, as seen in the leftmost image of Figure 2.3, the FKFS Swing [9] TGS which uses oscillating airfoils, seen in the center image of Figure 2.3, or active grids which

utilize rotating diamond-shaped grid elements. An example of an active grid can be seen in Figure 2.6 where flat diamond shaped plates are affixed to rods that run the width and height of the test section nozzle. Attached to each of the rods are stepper motors used to control the velocity and direction of the rotations of the rods. Active grids, which is the focus of this research, utilize their rotating elements to vary the blockage to increase the turbulence intensities and local Reynolds number [41]. This in turn produces larger length scales than a passive drag-based systems.

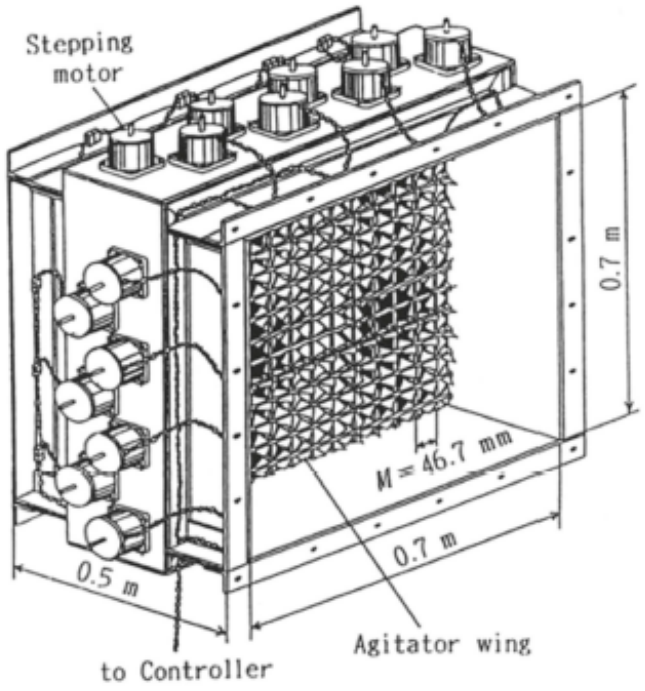

Figure 2.6: Schematic of Makita's active grid showing 15 vertical and horizontal shafts with corresponding stepper motors and grid elements [42]. Reprinted with permission.

Active grids were first motivated by a desire to achieve a sufficiently clear inertial subrange in order to replicate high Reynolds number turbulence conditions, such as atmospheric flows, in scaled wind tunnel tests [37] which would only be possible in high Taylor Reynolds number turbulence. The active grid design was first developed by Makita in 1991 [37] which is shown in Figure 2.6. In the design, diamond-shaped grid elements were affixed to 15 vertical and horizontal rods giving a mesh length of 46.7 mm. The active grid was able to achieve a relatively high Taylor Reynolds number of $\mathrm{Re}_\lambda = 387$. The relatively high Re_λ caused the inertial subrange to exist over two decades, which would not be possible with a traditional passive grid. For the same system, when operated in passive mode, wherein the rods were stationary and the blockage of the grid elements were minimized, a similar inertial subrange could not be identified, as shown in Figure 2.7, and the corresponding value of Re_λ was 34 [43]. Makita states that the inertial subrange could not be observed in the energy spectra when the $\mathrm{Re}_\lambda < 250$ [37]. Since the measured on-road Taylor Reynolds number is often on the order of $\mathrm{Re}_\lambda \geq 10^4$ [16], and therefore exhibiting a distinct inertial subrange, an active grid over a passive grid is desirable to replicate the turbulent flow field in controlled wind tunnel tests. However, most laboratory research wind tunnels are limited to a local Reynolds number of $\mathrm{Re}_\lambda = 10^3$ due to size [44]. Most active grids to date have been limited to $\mathrm{Re}_\lambda < 1000$; however some authors have been able to exceed this value [44–46] with Bodenschartz et al. [35]

producing a local Reynolds number of $\mathrm{Re}_\lambda = 1620$ in their variable density wind tunnel, some of the highest values produced by an active grid.

Various forcing protocols have been used to study a range of flows such as homogeneous isotropic turbulence [18, 44, 45, 47–53], shear turbulence [54, 55], and to reproduce atmospheric turbulence conditions [56–58]. Some authors have also investigated the effect of the initial condition of the operating protocol on the generated turbulence [18, 45, 59], where the operating protocol describes the parameters of how the system is driven.

Mydlarski [15] summarized three main classifications of the modes of operation of an active grid, based on an earlier review by [49]. The three modes of operation are given as (a) synchronous, (b) single-random and (c) double-random. In the synchronous mode, all the rods rotated at the same angular velocity with adjacent rods rotating in opposite directions [47]. The single-random mode would rotate all of the rods at the same angular velocity, however the direction of rotation would alternate after a random period of time [37, 47]. The double-random mode randomizes the magnitude of the rotational rate as well as the time period before switching direction [18, 45, 48].

Most active grids use bars that run the full height and width of the nozzle with flat grid elements mounted to the rods, however recently some authors have attempted to increase their systems degrees of freedom to provide an even greater

level of control. One of the largest active grids in use to date uses rods that are split along the vertical and horizontal center lines to allow for 80 independently controllable rods [57]. The only other active grid with a greater degree of freedom, to the authors knowledge, is the active grid discussed in [35] with 129 independently controllable grid elements, each with its own servo motor attached to the grid element. Herbert et al. [59] used a similar design with servo motors mounted to the grid elements, however their design was much smaller with only 24 degrees of freedom. The added flexibility of independently controllable grid element was shown to improve the homogeneity of the generated turbulence [59].

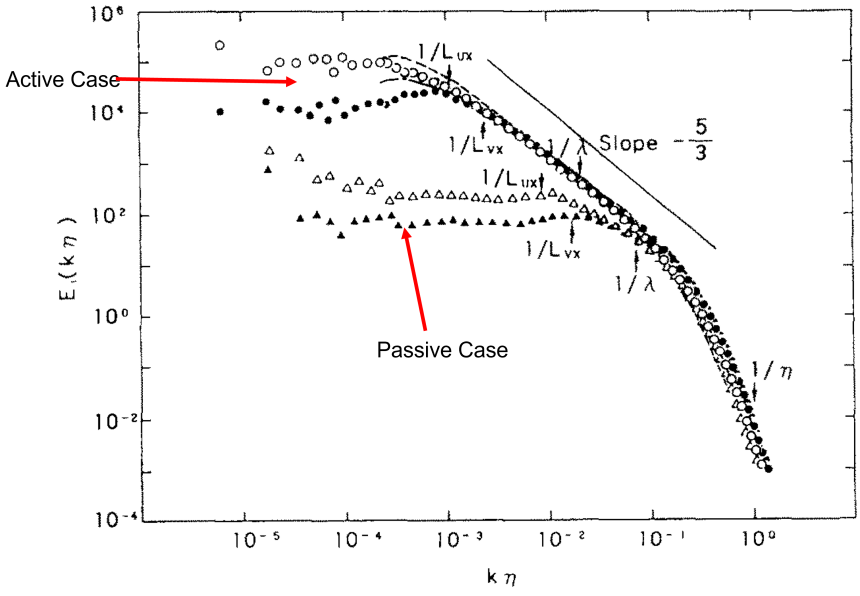

Figure 2.7: Spectra produced by Makita's [37] active grid operating in different modes including passive and active. Reprinted with permission.

Makita [37] shows that active grid systems can be plagued by anisotropic ratios of 1.8 just behind the grid and in the case of their grid, this ratio did not reduce to < 1.3 until more than $X/M > 50$. To improve this anisotropy ratio, he suggested the use of a slight secondary contraction to stretch the longitudinal scales, lowering the anisotropic ratio closer to unity. Larssen and Devenport [45] tried this by placing their active grid in the contraction of their wind tunnel where they were successful in reducing the anisotropic ratio down to near unity while achieving a local Reynolds number of $\mathrm{Re}_\lambda = 1360$.

Active grids are capable of producing a wide range of length scales and intensities. There are two key non-dimensional parameters with respect to an active grid that have been found to be most influential in producing turbulence [18] and one geometric parameter. These are:

- The Rossby number - defined as $\mathrm{Ro} = U/(\Omega M)$, where U is the mean velocity, Ω is the rotational rate of the grid elements, and M is the mesh size.
- Grid Reynolds number - defined as $\mathrm{Re}_M = UM/v$ Where v is the kinematic viscosity.
- The grid element geometry - specifically pertaining to the physical shape, and size of the grid elements as well as the overall blockage of the grid.

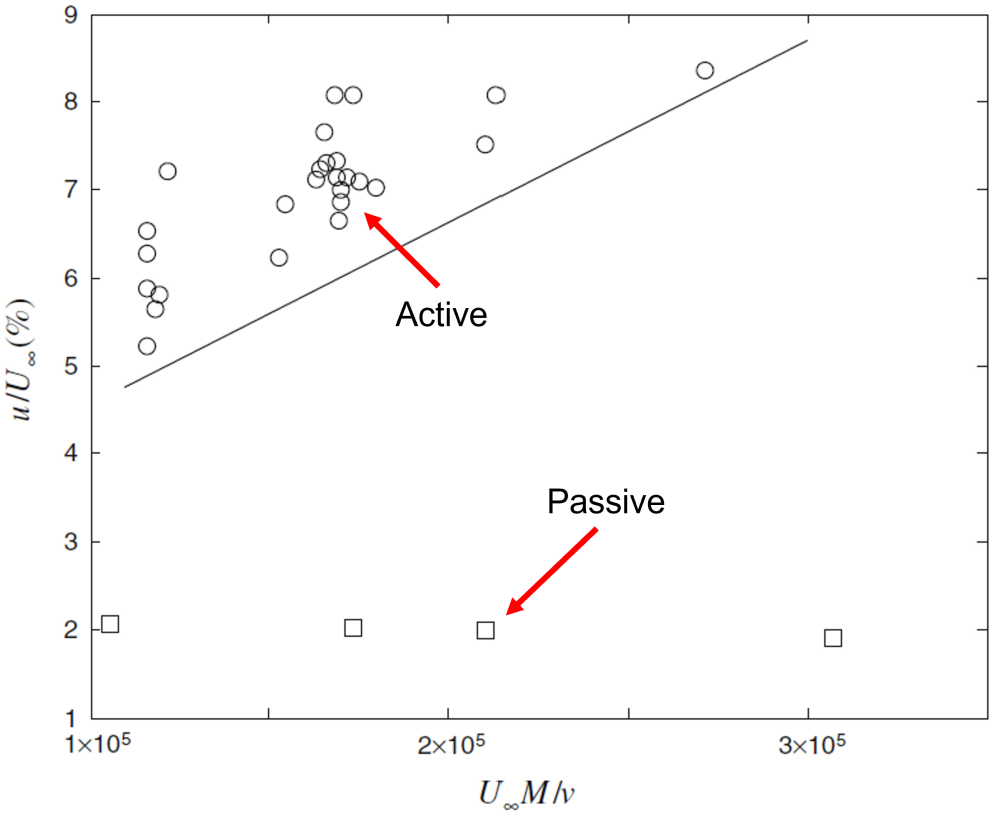

Figure 2.8: Turbulence intensity plotted against grid Reynolds number. Circle symbols represent the grid in active mode while squares represent the grid in passive mode [45]. Reprinted with permission.

Larssen and Devenport illustrate how the grid Reynolds number affects the turbulence intensity in Figure 2.8 [45]. In this experiment, Larssen and Devenport ran their system in both an active and passive mode where the measurement location was fixed and only the velocity was varied to demonstrate how the grid Reynolds number affects the turbulence intensity in each case. It can be seen that the intensity continues to grow as the grid Reynolds number grows for the active

case, however the turbulence intensity remains fairly low and flat when the system is operating in the passive case. In addition, Hearst and Lavoie [18] showed that the turbulence characteristics of an active grid have a great dependency on the Rossby number. They found that by varying the Rossby number, the size of the large turbulent scales could be manipulated while keeping the turbulence intensity fairly constant by varying the rotational rate, as can be seen in Figure 2.9. In fact, over the range of $50 < U/\Omega M < 175$ the length scales continued to grow by a factor of 3.5 times by varying only the rotational rate. Figure 2.9 depicts this trend of varying turbulence intensity and length scales with Rossby number for 3 different vane geometries. The different vane geometries are shown on the right side of Figure 2.9 with the standard flat and solid diamond shaped vane shown in red, a flat diamond vane with two circular holes cut into the vane to decrease the blockage shown in black, and a flat circular vane shown in blue.

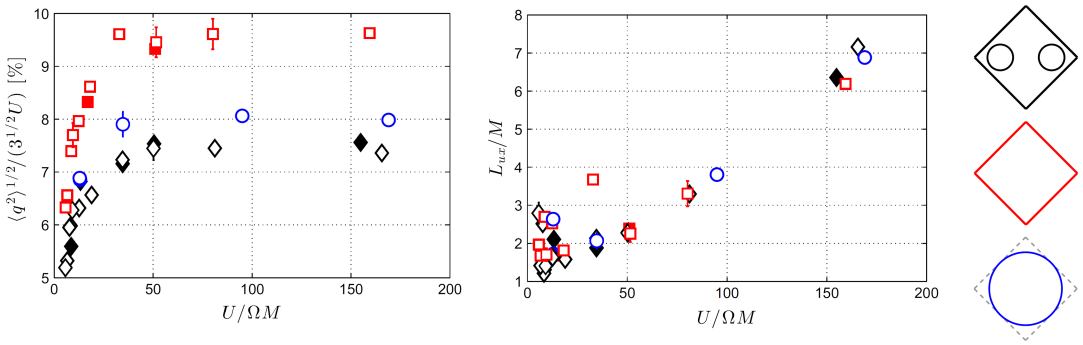

Figure 2.9: Variation of the turbulence intensity (left) and turbulence length scale (right) with Rossby number [18]. Reprinted with Permission.

3 Turbulence System Design

This chapter provides an overview of the design of the TGS, with main focus on the active grid. However, given the overlaps associated with the three subsystems, reference is made to the unsteady flow system and active yaw system where required. The contributions to the developement of the system by the author include the design and building of the active grid and gusting system as well as the design and assembly of the cassette housing. The manufacturing of the cassette housing was done by Ryan's Custom Machine in Toronto, Ontario. The active yaw system that integrates with the active grid system was designed and assembled by a fellow Master's student Germiel Cacho. Both the active grid vanes and the yaw system airfoils were 3D-printed by Agile Manufacturing in Beaverton, Ontario. Modifications to the wind tunnel to accept the TGS were performed by the author.

3.1 Prototype Vane Designs and Simulations

As previously explained, the novel TGS considered within this thesis has three distinct subsystems that are meant to be individually operable, which is distinct feature separating it from traditional active grid systems. The active grid system is meant to also operate as a fully open passive configuration to permit individual operation of the unsteady flow system and yaw system. In addition, the fully open state of the grid will act as a low turbulence level passive system. As a result, the simple common element design, a flat plate element mounted to a rod [18, 37, 50], can be improved for the requirements of the current system. As such, the evaluation of different grid element geometries was investigated. Figure 3.1 presents four of the diamond shaped designs that were considered. The diamond shape is used as the vanes are designed to fit together to form an almost "solid" mesh as shown in Section 3.3. The front and side profiles can be viewed as well as the isometric view of each of the models. It should be noted that these grid element geometries were considered as their small size makes them amenable to 3D printing, otherwise the geometries presented would not have been economical to manufacture.

Flow simulations were performed to analyze the behaviour of low-profile grid elements that could be manufactured using 3D printing technology. The simulations serve only as a design guide to choose a geometry giving suitable performance

characteristics from the distinct options shown in Figure 3.1. The CFD simulations were performed using the commercial code Star-CCM+. The flow was simulated using the coupled implicit incompressible finite-volume solver with a second-order upwind scheme to discretize the convection and diffusion terms. Turbulence quantities were modelled using the realizable $k - \varepsilon$ equations and two-layer wall model.

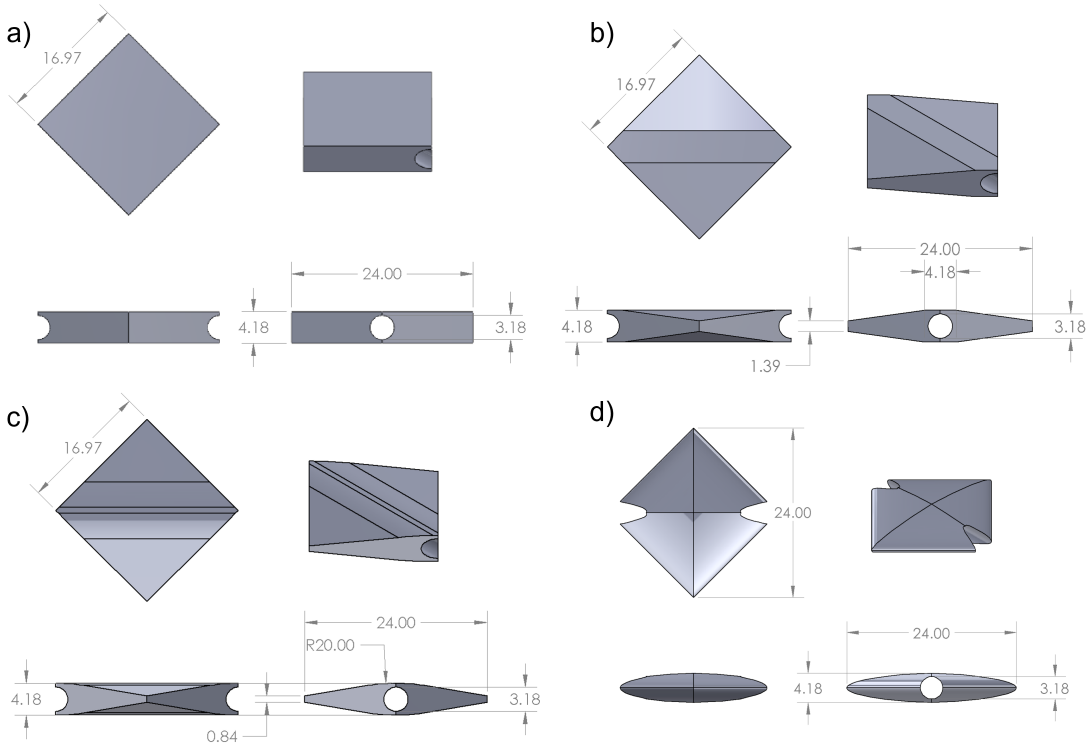

Figure 3.1: CAD models of the a) Flat, b) Tapered, c) Tapered Sharp, and d) Rounded grid element designs. Dimensions are given in units of mm.

CFD simulations were completed in Siemens Star-CCM+ with the grid elements

at varying angles of attack from 0° to 44° at 27 m/s. The domain, seen in Figure 3.2, measured approximately 40W x 3W x 12W (LxWxH) where W was the width of the vane of 24 mm. The base size of the mesh was 25 mm with a larger refinement mesh of 12.5 % of the base size and smaller refinement mesh of 6.25 % of the base size. An additional wake refinement region was also added to the grid element model. The inlet of the domain was set as a velocity inlet while the outlet was set to a pressure outlet. The sides of the domain were set as symmetry planes while the top and bottom of the domain were set as walls with a slip condition.

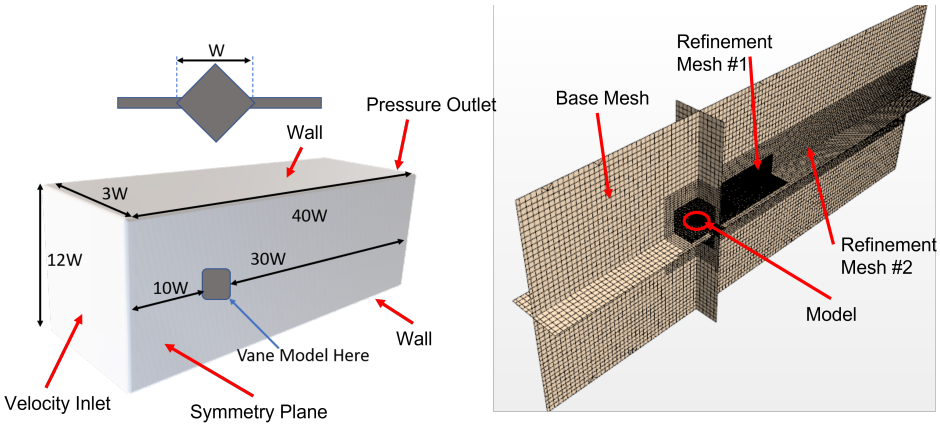

Figure 3.2: The dimensions of the domain used in the CFD simulations as a function of the grid element width.

A mesh independence study was completed on the flat baseline model at two angles of attack (AoA), 0° and 20°. The base sizes tested were 18.75 mm and 50 mm to view how the metrics of interest, the lift and drag, varied with mesh size. For the model at 0° AoA model, the coefficient of drag changed by 2 % going from

a 50 mm base mesh size to a 25 mm base size. However, from 25 mm to 18.75 mm base size the coefficient of drag changed by only 0.67 %. Comparisons made for the three meshes with the element geometry rotated to a 20 degree AoA showed almost identical changes in the drag coefficient for the corresponding reductions in the base mesh size. It was concluded that 25 mm was an acceptable base size as further reductions in size did not produce appreciably different results for the lift and drag coefficients, however would significantly increase the computation time. A summary of the mesh dependency results are shown below in Table 3.1.

Resolution	Low		Medium		Fine	
AoA	0°	20°	0°	20°	0°	20°
Base Mesh (mm)	50	50	25	25	18.75	18.75
Number of Cells	0.63M	0.68M	3.69M	4.12M	8.14M	9.05M
C_d	0.302	0.476	0.296	0.473	0.298	0.477
C_l	$4e^{-4}$	0.424	$8.6e^{-5}$	0.419	0.422	$5.25e^{-2}$

Table 3.1: Summary of mesh dependency study results for the Flat grid element geometry at 0° and 20° angle of attack.

The Rounded grid element showed a very low drag coefficient throughout the tested AoA range, especially at 0°, which was of particular interest. However, its drag coefficient remained much lower than the other models throughout the tested AoA range which was undesirable since higher drag would generally produce a larger wake contributing to higher turbulence levels. The tapered type grid elements had a more linear lift coefficient without the steep drop-off that the rounded vane had

indicating that the point where the flow was separating from the vane was likely independent of the angle of attack thanks to its sharp corners. While it did not have the same low drag coefficient at 0° that the rounded grid element had, it was still a noticeable improvement over the flat grid element's drag coefficient at the same angle. Lastly, a hybrid of these two models was tested, with rounded faces, but flat leading edges with sharp corners. The results for this model can be seen in Figure 3.3 labelled as the Blunt Rounded element. The inspiration for this design pulled from aspects of the rounded grid element as well as the tapered type elements with sharp edges. The rounded faces would encourage the attached flow to stay attached and minimize the drag at low angles of attack as seen in the rounded vane, while the sharp flat leading edges would encourage the flow to separate as the vane moved to higher angles of attack, akin the behaviour seen in the tapered grid element. A detailed example of this design can be seen in Figure 3.5 in Section 3.2. While this model does not have an obvious stall point until late in the tested AoA range, it produced a much higher drag coefficient than any of the other designs, even surpassing the "baseline" Flat grid element case. The Blunt Rounded design was selected as the base element design of the active grid.

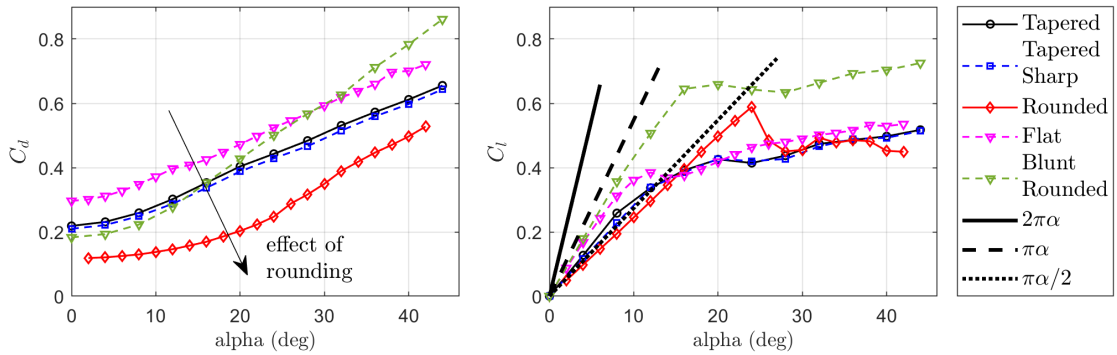

Figure 3.3: Results of CFD simulations for five of the grid element geometries tested over a range of angles of attack.

3.2 Vane Assembly and Prototyping

Manufacturability had a major impact on the designs of the grid elements for this active grid system. Due to the small size of the elements, 16.6 mm square, and their rounded nature, most manufacturing processes would have been impractical. As such, Multi Jet Modeling 3D-printing was selected as the method for the grid elements which were then slid over a 3.175 mm diameter steel rod and aligned using a 3D-printed jig. Super glue was injected into the grid elements through 0.5 mm channels using a hypodermic needle. Several grid element prototypes were 3D printed, an example of the 3D-printed jig and prototype grid elements is shown in Figure 3.4. The prototypes were used to verify aspects of the design including acceptable rigidity, surface finish and the glue channels.

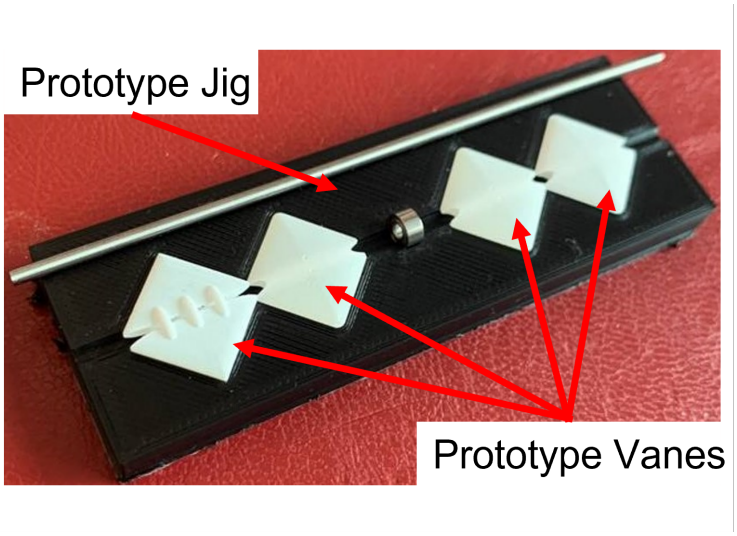

Figure 3.4: Prototype jig designed to aid in the alignment and spacing of the vanes and bearings along the steel shaft.

The active grid was designed as part of a system that also included active yaw generation using twelve airfoils. The airfoils effectively eliminated a vertical rod that would otherwise be used for active grid elements. Whereas standard symmetric diamond shaped elements (shown in Figure 3.5) were used on the vertical rods, the horizontal elements (shown in Figure 3.6) were made asymmetric to increase blockage near the airfoils of the active yaw system. This will be discussed further in Section 3.3.

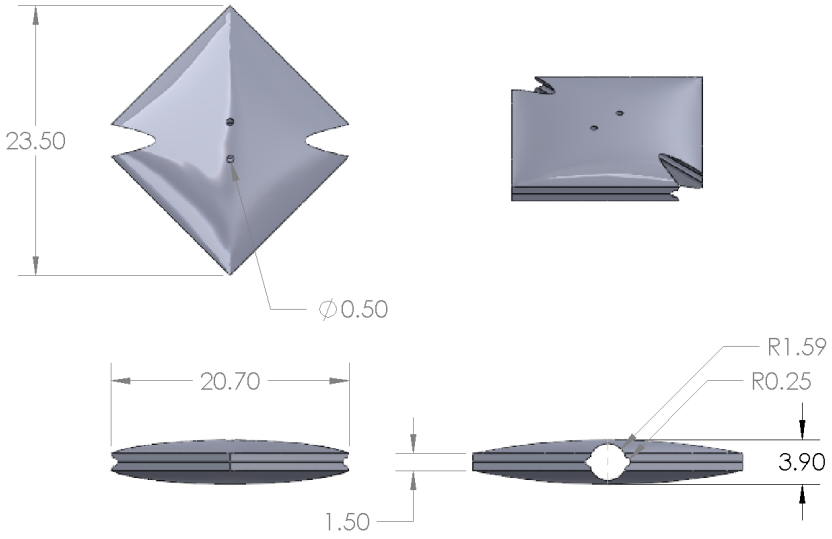

Figure 3.5: The final vertical grid element design CAD model. Dimensions of units are in mm.

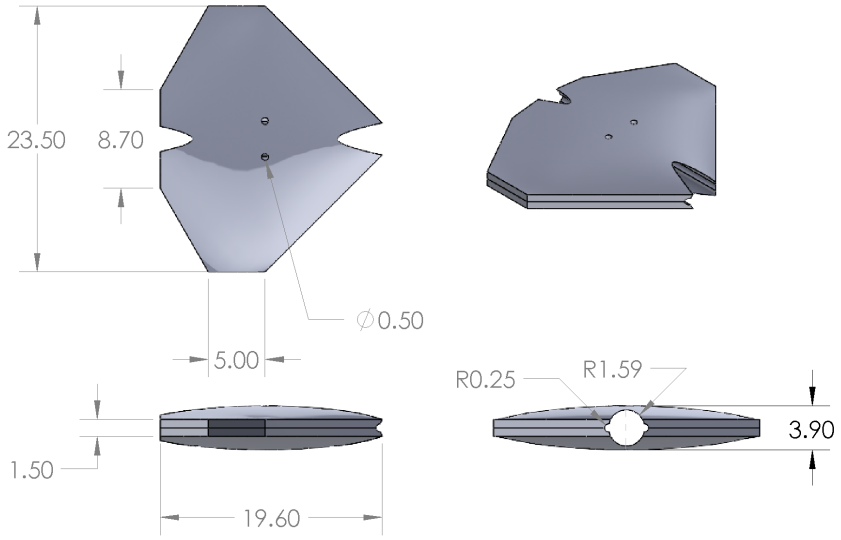

Figure 3.6: The final horizontal grid element design CAD model. Dimensions of units are in mm.

3.3 Active Grid

The active grid was designed to accommodate a 12-airfoil yaw system, and therefore every other vertical active grid assembly is essentially missing where an airfoil resides. To compensate for the reduced blockage around the airfoils, the horizontal grid elements were designed to be wider on the side adjacent to the airfoils to increase their blockage. The vertical active grid assemblies still utilize the classic diamond shape seen in literature [18, 37, 45, 50]. A CAD model of the two systems can be seen together in Figure 3.7. In this configuration with the active grid in its fully closed position, the total blockage is approximately 89 %. The colours denote the different axes that the grid elements are mounted to. Blue elements are mounted to the horizontal rods, purple elements are mounted to the upper vertical rods, and the yellow elements are mounted to the lower vertical rods. The vertical rods have been decoupled to allow for actuating the upper section independently of the lower section. This was done to give the flexibility of introducing streamwise pulsations into the flow similar to what is found in the Toyota TGS [10] by opening and closing the upper porting of the grid. The grid can theoretically gust the flow by as much as 18 % based on the conservation of mass for the area change during a gust. An example of the grid fully open and in full gust can be seen in Figure 3.8. The systems blockage in its fully open and full gust positions is approximately 27 % and 45 % respectively.

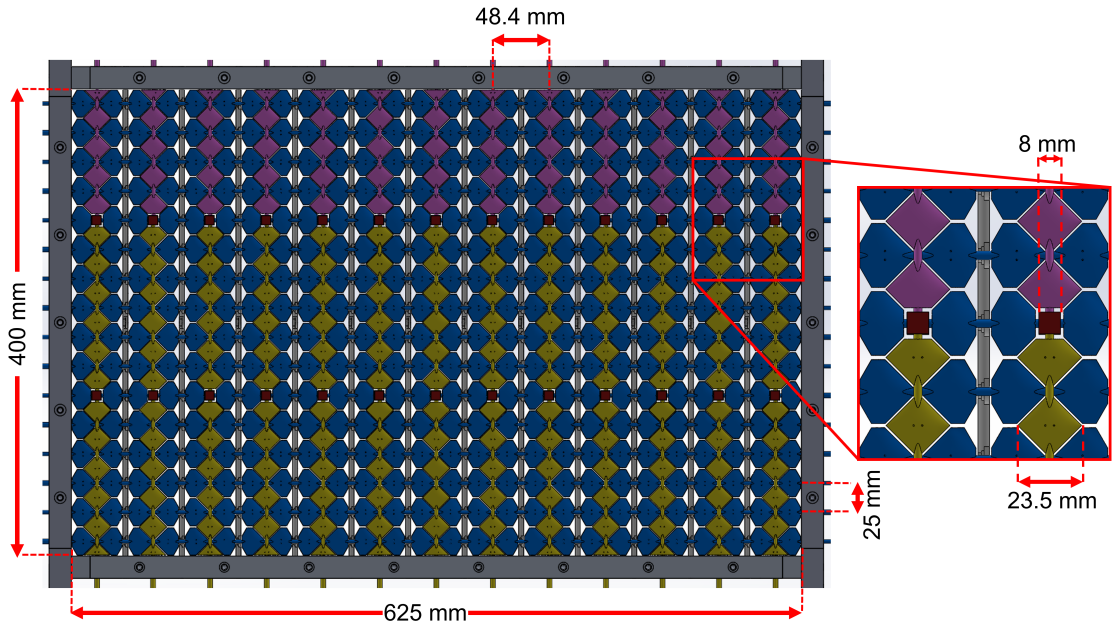

Figure 3.7: CAD model of the active grid and active yaw system coupled together (left) as well as a zoomed in image of the elements (right).

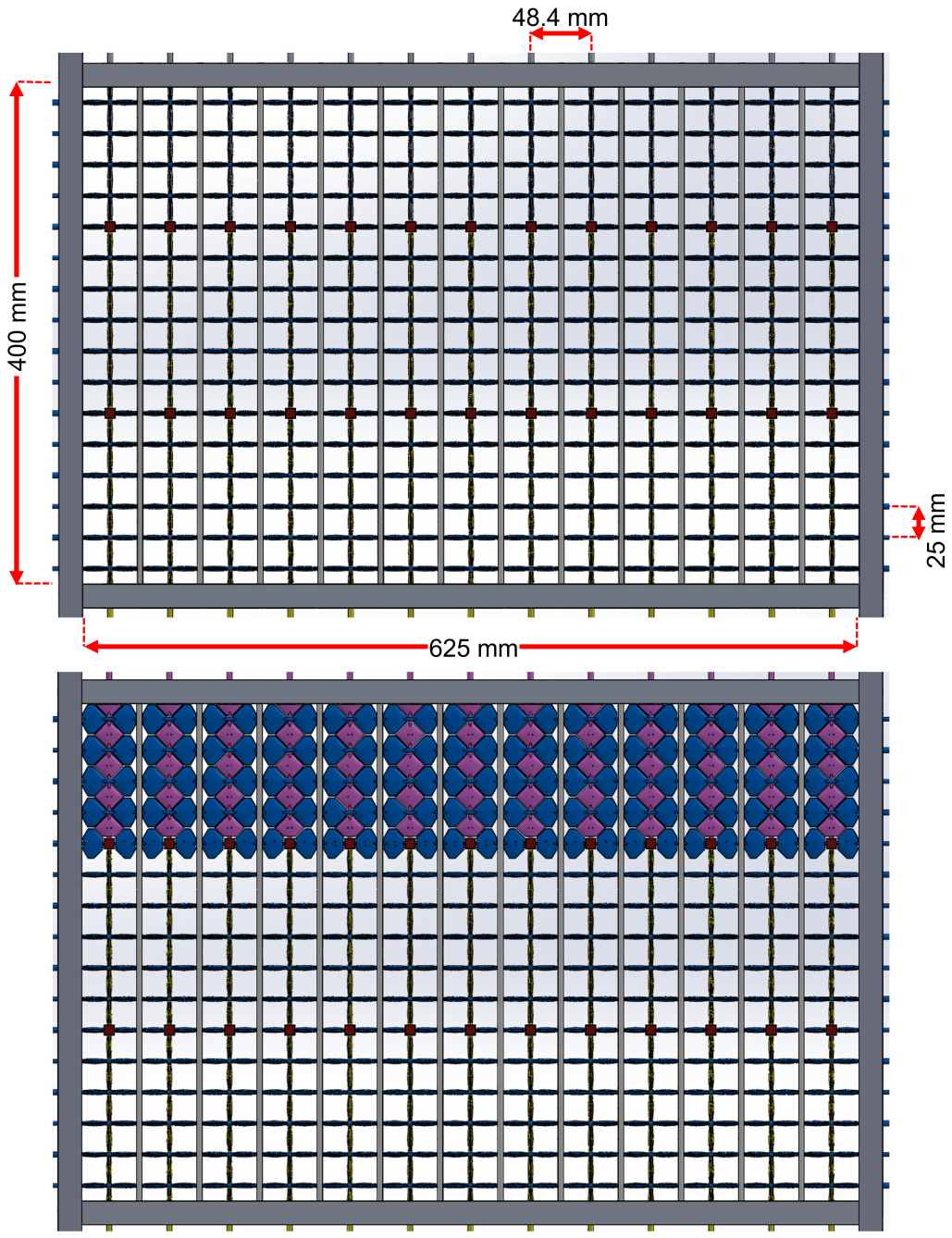

Figure 3.8: The TGS in the fully open position (top) and with all the upper elements shown closed for simulating a gust (bottom).

Due to the aspect ratio of the nozzle of the wind tunnel of 16:25, as well as the spacing between each of the 12 vertical airfoils, the active grid does not have equal mesh length in the vertical and horizontal directions. The horizontal mesh spacing is 24.2 mm while the vertical mesh spacing is 25 mm. All further references to mesh length herein refer to the mesh length of 25 mm. Figure 3.9 shows the TGS installed onto the nozzle of the testing section. The grid assembly includes an additional riser plate (seen on the left side of the grid) for a second row of motors used for actuating the yaw system. The additional row of motors for the yaw system are not installed in Figure 3.9. The floor of testing section (seen on the left side of Figure 3.9) was replaced with a large acrylic window to provide optical access to the testing section as well as to allow for visual inspection of the setup and future Particle Imaging Velocimetry (PIV) measurements.

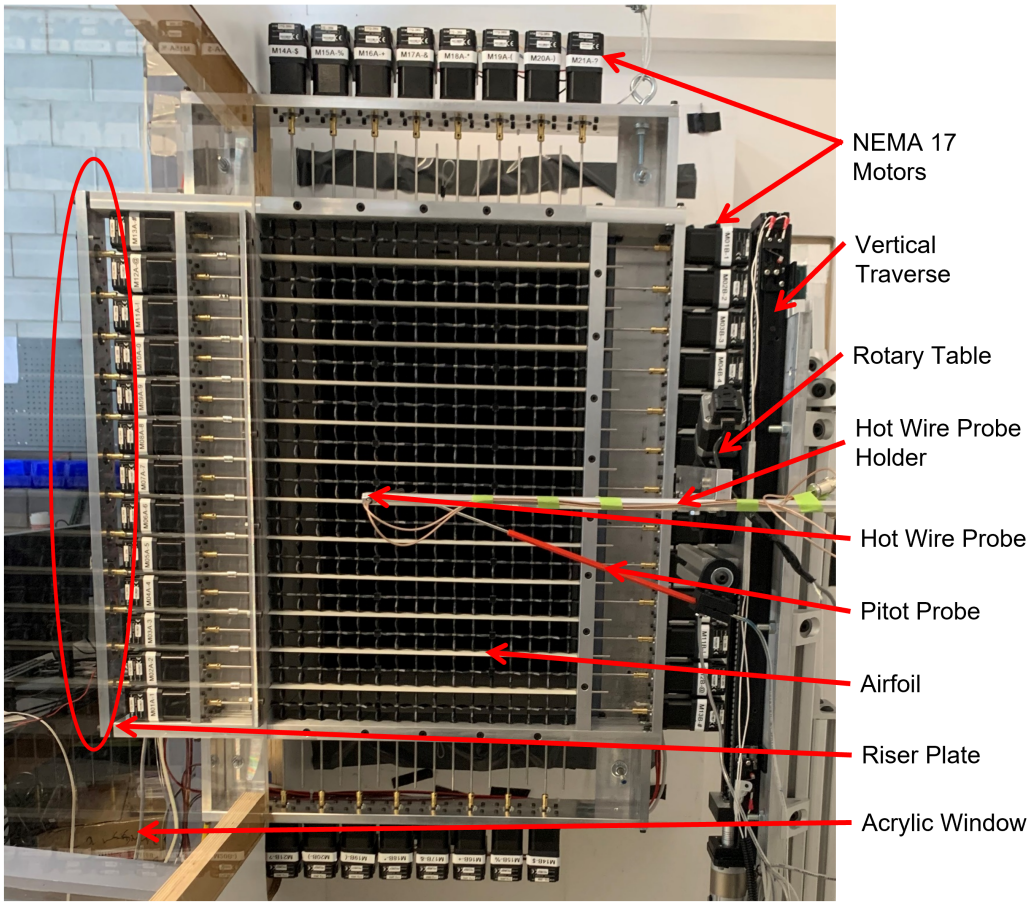

Figure 3.9: The TGS installed in the testing section of the wind tunnel.

The grid utilizes 611 grid elements mounted to 16 horizontal and 26 vertical 3.175 mm diameter steel rods, actuated by 42 STM17Q-3RN integrated stepper motors from Applied Motion, capable of rotational rates up to 50 Hz. Each of the vertical and horizontal grid element assemblies were assembled using 3D-printed jigs (seen in Figure 3.4), to achieve the correct spacing and alignment of the grid

elements. Support blocks, seen in red in Figure 3.7, link the vertical assemblies to the horizontal assemblies. The 8 mm x 8 mm support blocks were designed as small as possible while still being able to accommodate a R-144ZZ bearing. Figure 3.10 shows the support block being glued together during the assembly process. The white bars in the figure are the bodies of the airfoils from the yaw system without their flaps installed. Within each of the airfoil bodies is a bearing for the horizontal active grid assemblies where they pass through.

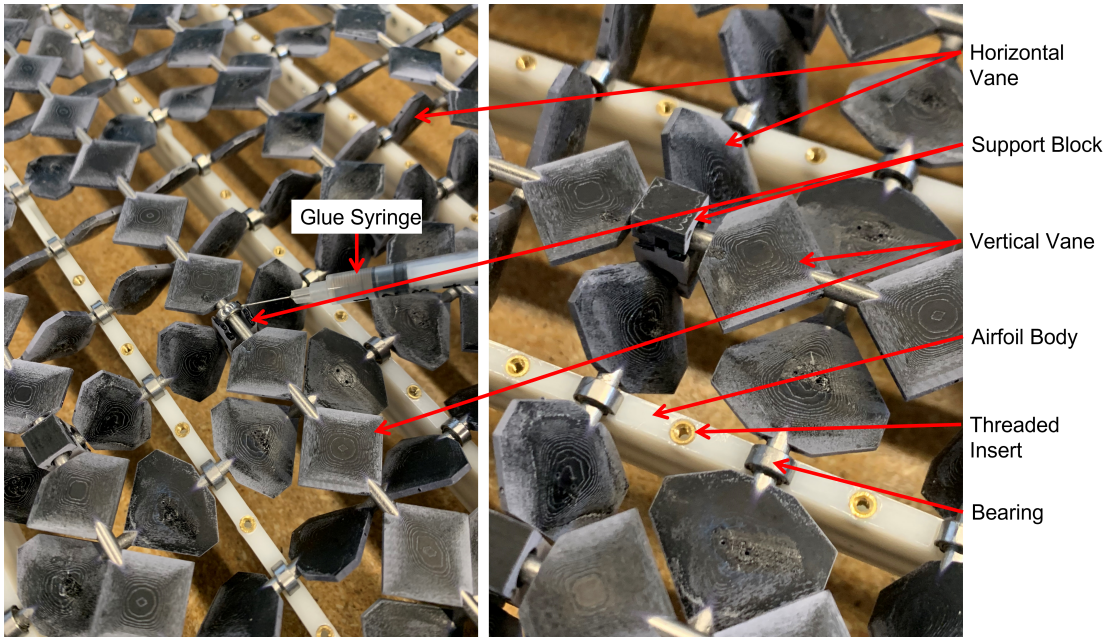

Figure 3.10: Image of the active grid and active yaw system coupled together (left) as well as a zoomed in photo of the elements (right) during installation of the active grid elements.

3.4 Cassette Housing

The active grid cassette housing was designed to accommodate both the active grid and the active yaw system together. However, the system was designed such that the active grid can be removed from the cassette housing without removing and dismantling the entire cassette housing. This was done to allow for the ability to quickly and easily service the grid should the need arise, but also so that the wind tunnel can operate without the active grid installed. Figure 3.11 shows the front of the cassette housing with one of the front clamping plates removed illustrating how the active grid could be removed from the housing assembly without disassembling the housing.

Supporting each of the rods where they pass through the cassette housing are R-144ZZ bearings with a square-profile O-ring placed over them. The O-ring was used to apply even pressure by the housing to the bearing so that it is secured in place. This method for securing the bearings had the added benefit of reducing the dimensional tolerance on the machined parts.

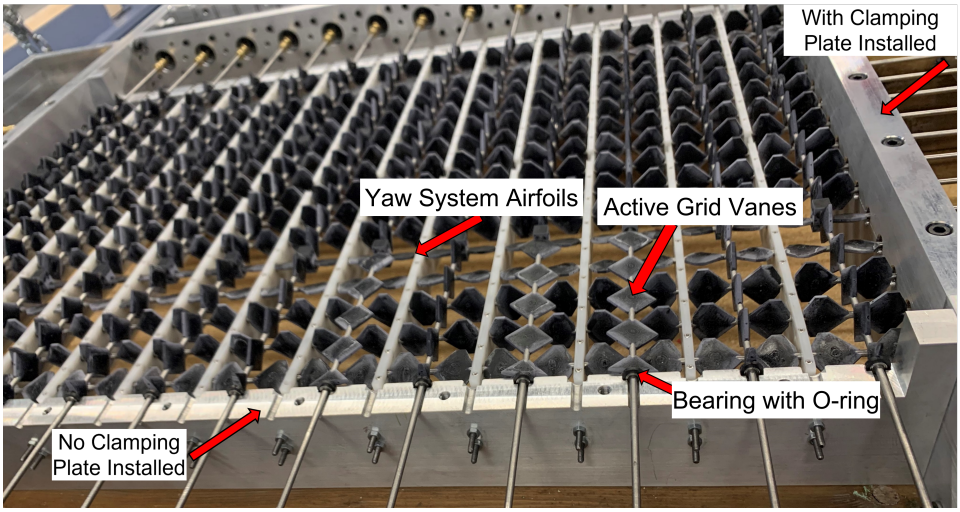

Figure 3.11: Cassette housing with and without the clamping plates installed.

The housing was affixed to the wooden nozzle of the test section using a combination of methods. The majority of the weight is supported by steel cables that run down from the ceiling of the test section and attach to a pair of eye bolts on the cassette housing. This prevents undue loading on the nozzle of the wind tunnel. Secondly, the housing was bolted to the front of the nozzle using custom aluminum brackets. The brackets not only holds the grid on firmly to the nozzle, but it also was used to align the grid with the nozzle to ensure a smooth transition from the nozzle to the housing. Lastly, each of the four corners of the cassette housing has a threaded rod that is used to squeeze a thin gasket between the nozzle and grid prevent possible air leakage.

4 Experimental Facility and Methods

4.1 Wind Tunnel

The BMW-Aiolos wind tunnel that was used in the following experiments is a 1:10 scale model of a full sized automotive wind tunnel. The wind tunnel is a low-speed, closed circuit 3/4 open-jet design where the testing section is essentially open to a room on three sides and vented to atmospheric pressure. The open room of the open-jet allows the air to flow around a blockage, such as a vehicle in the flow, as needed without causing the flow to speed up due to the blockage. This allows for flow behaviours that are more akin to what is observed on the road. Without the active grid system installed, the wind tunnel is capable of reaching an approximate mean flow velocity of 70 m/s, however with the added pressure loss added by the active grid, the fan blades were re-pitched to overcome the added pressure loss. A top-down drawing of the wind tunnel can be seen in Figure 4.1 where the testing section can be seen near the bottom of the image. The model wind tunnel used in this thesis has been built on its side to allow the operator easy access to all areas

of the tunnel. This means that the "floor" of the testing section is actually a wall to an observer.

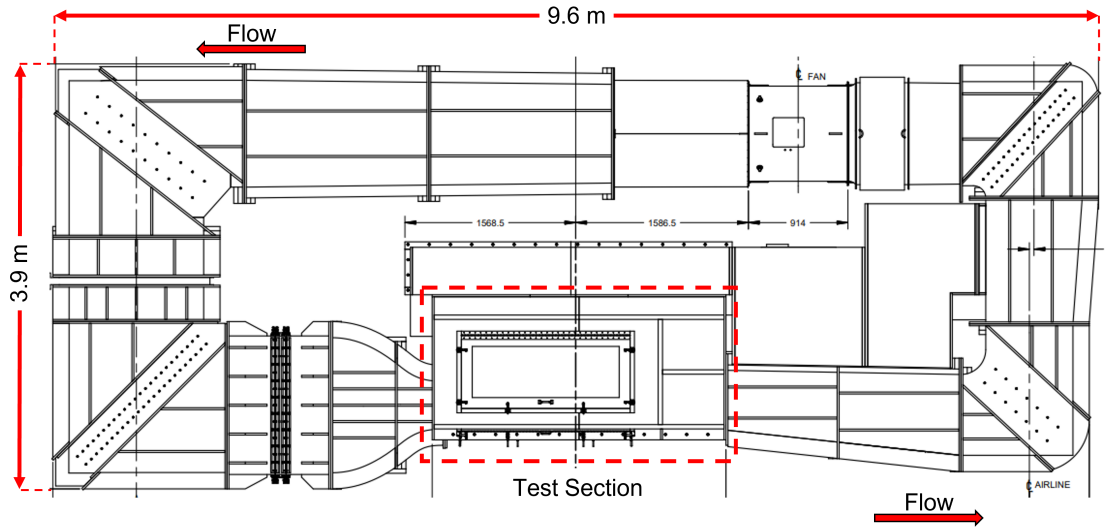

Figure 4.1: Schematic of the 3/4 open-jet closed loop wind tunnel used in the present research, with the test section highlighted.

4.2 Instrumentation

Measurements of the flow velocity in the time domain were made using two-component (or x-wire) hot-wire anemometry. The wires of the Dantec model 55P61 hot-wire probe was used to measure the streamwise (u) and transverse (v) velocity components. x-wire probes use two wires oriented 45° to the oncoming flow and perpendicular to one another, allowing for each wire to be cooled at different rates depending on the angle of the oncoming wind. This enables the x-wire

probe to measure two components of the flow simultaneously [60] allowing for both the velocity and the angle of the flow to be determined. Constant temperature anemometers measure the velocity of a flow by measuring the voltage required to maintain the 5 μm diameter gold-plated wire at a specified temperature [61]. Because of their very small diameter, x-wire probes tend to have a rapid response time making them well suited to measure the rapid fluctuations of a turbulent flow. The x-wire probes were set with an overheat ratio of 0.7 and and internal offset of 1.182 V with a gain of 8 on the Dantec StreamWare Pro system.

The x-wire probe was calibrated before and after each test run to minimize the effect of drift on the measurements. Calibration of the x-wire probe was done in-situ at 30 mesh lengths downstream of the grid and with the grid fully open. The look up table method was used for the calibrations [60, 62] in which the wind tunnel set to a fixed known velocity (measured by a pitot probe), and then the x-wire probe is pitched through a set of known angles. The process is repeated for several other flow velocities. The time-average voltages from the x-wire probe, E_1 and E_2 (one for each wire in the probe) are recorded and used in conjunction with a cubic spline interpolation to calculate grid points corresponding to unique flow angles and velocities.

For the calibrations conducted in this thesis, the probe was pitched in 5° increments from -30° to +30° for 11 wind velocities ranging from 5 - 29 m/s. The

mean flow velocity was provided by a FCO65 pitot pressure probe from Furness placed beside the x-wire. The pitot probe was connected to a differential pressure transducer, Honeywell HSCDRRN002NDAA5, with an operating pressure of ±0.5 kPa and an accuracy of ±1.25 Pa. The pressure transducer outputs a voltage signal which can be converted to the dynamic pressure by

$$P_{applied} = (V_{out} - 0.1 * V_{supply}) \frac{P_{max} - P_{min}}{0.8 * V_{supply}} + P_{min}$$

where V_{out} is the voltage output from the sensor, P_{min} and P_{max} are -500 Pa and 500 Pa respectively as given by the manufacturer, and V_{supply} is 5 V from the power supply to the sensor verified by a multimeter. From there, a simplified form of Bernoulli's equation is used to convert the pressure to a free stream velocity

$$U_\infty = \sqrt{\frac{2(P_0 - P_\infty)}{\rho}}$$

where P_0 is the total pressure and P_∞ is the static pressure. Before and after each calibration, the pressure sensor voltage was recorded when the wind tunnel was off to compensate for potential zero offset in the sensor.

However, before the look-up table can be applied to experimental data, the output voltages from the x-wire probe are corrected for fluctuations in the air temperature during the experiment. The temperature data was sampled from the outlet of the test section using an Omega DPi16A-C24 signal conditioner with a T-type thermocouple with an accuracy of 2 %. From there, the corrected CTA

voltages can be calculated by

$$E_{corr} = E_a \sqrt{\frac{(T_w - T_0)}{(T_w - T_a)}}$$

where E_a is the acquired voltage, T_w is the sensor hot temperature, T_0 is the ambient reference temperature (recorded during overheat setup), T_a is the temperature recorded by the thermocouple, and E_{corr} is the corrected voltage. During the experiments in this research, the temperature of the air within the wind tunnel was maintained to ± 1°C through the use of an air-to-water heat exchanger upstream of the settling chamber. The pre- and post-calibration look-up tables were linearly weighted when applying them to raw experimental data to mitigate the possible drift of the x-wire. However, the average difference between the pre- and post-calibrations was typically 0.5 %.

The image on the left in Figure 4.2 shows a x-wire probe next to the pitot pressure probe at a 0° angle of attack, which is the angle the probe is held at during experiments. The image on the right in Figure 4.2 shows the hot-wire probe holder rotated at 30° illustrating how a calibration would look.

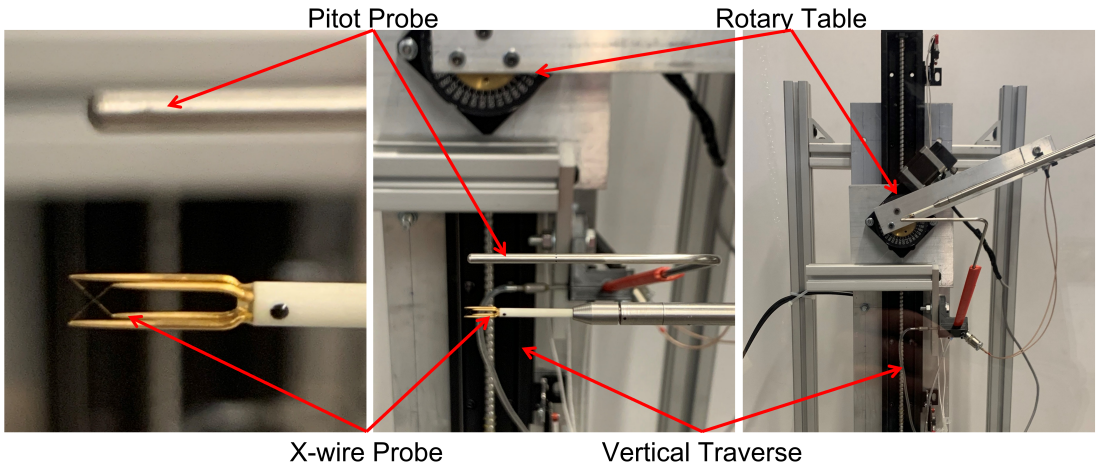

Figure 4.2: (Left) Close up of the x-wire and pitot probe. (middle) The x-wire probe installed in the wind tunnel next to a pitot probe used for calibration. (Right) The x-wire probe holder rotated at 30° while the angle of the pitot probe remains unchanged.

Before beginning experiments, testing was done to determine sampling duration of each measurements to ensure that sufficient independent samples were taken at each point to obtain a converged mean. This was done by operating the grid in the *double random* mode (explained in Section 4.4) for different sampling durations. For sampling period of 180 s, the maximum uncertainty measured 1.3 %. Further increasing the sampling period did not appreciably reduce the sampling error. The calculation for the uncertainty can be found in Appendix C.

Furthermore, rough and fine mesh scans of the flow profile consisting of 215 and

187 points respectively were completed with the grid operating in a double random mode (4 ± 2 Hz) to view the flow profile caused by the active grid. An example of the turbulence intensity profile at 10M for the double random case can be seen in Figure 4.5. The RMS of the standard deviations in this Figure is 0.85 % indicating that the turbulence intensity distribution across the plane is fairly uniform apart from a few locations where the intensities were > 30 %.

After the scans, 10 points in the yz-plane were chosen that adequately represented the flow profiles that were captured during the scans. 10 points were chosen over a single point measurement location to give an average of the flow characteristics that a vehicle in the wind tunnel would see. 10 points also had the added benefit of mitigating potential nonuniformities in the wakes caused by the grid elements and airfoils of the TGS. In addition, the points were split into two lines of 5 points corresponding to the approximate height of the bumper and windshield of a vehicle in the wind tunnel. The mean velocities and turbulence intensities at each of the 10 points is shown in Table B.1 and Table B.2 in Appendix B respectively. An example of where the 10 points lie are shown in Figure 4.4. The mean turbulence intensity values are listed in Table 4.1 for the fine and rough mesh scans as well as for the 10 points that were selected. The selected 10 points were then used as the measurement points throughout the test cases. For each of the 10 points, the turbulence statistics were calculated and then averaged for an approximation of

the behaviour of the bulk flow. The averaged values of the 10 points are what are reported in this thesis.

Table 4.1: The mean intensity values for the rough mesh scan, fine mesh scan, and the selected 10 points at 10M.

	Rough	Fine	10 Points
u'/U (%)	28.4	29.3	28.9

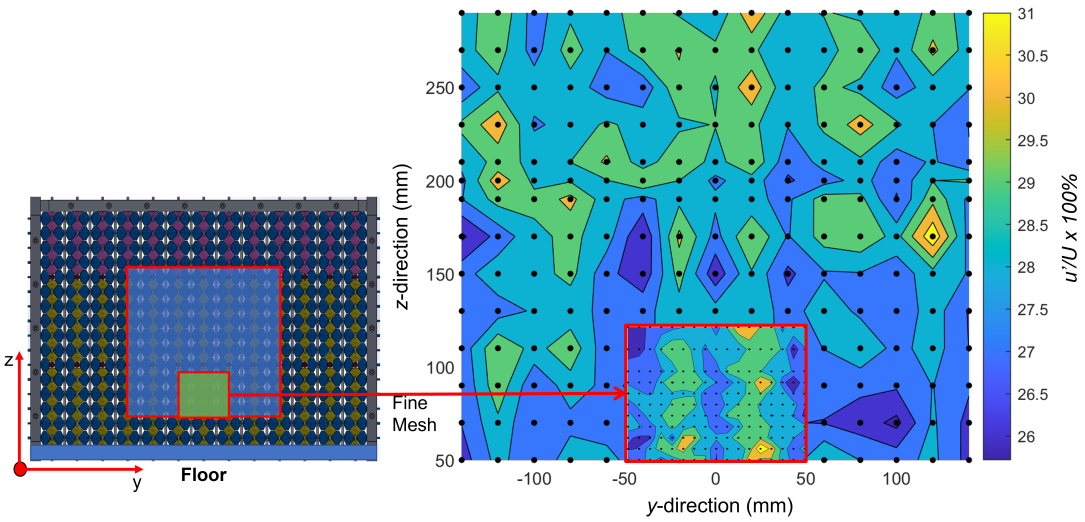

Figure 4.3: Turbulence intensity profile for the double random mode (4 ± 2 Hz) scan with the location of the rough mesh scan shown by the blue square and the location of the fine mesh scan shown by the green square. Measurement taken at 10M.

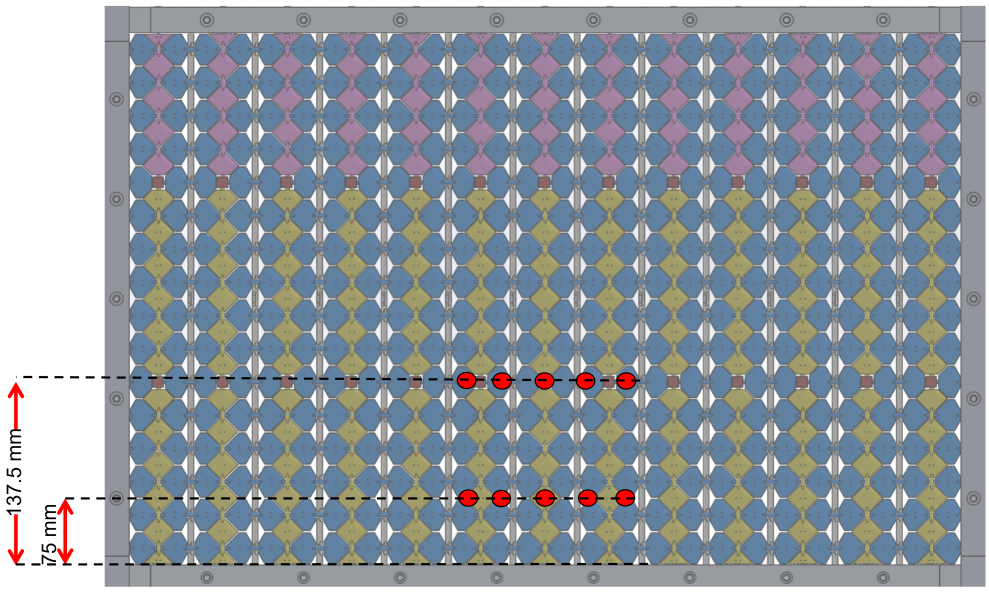

Figure 4.4: The ten points per streamwise plane that were chosen that adequately represent the turbulence intensity values collected during the rough and fine mesh scans.

The flow uniformity shown in Figure 4.5 is plotted in terms of U/U_{ref} where U is the mean velocity at each point, and U_{ref} is the mean flow velocity of all the points in the plane. In the rough scan portion of Figure 4.5, it is evident that there appears to be a gradient in the flow velocity, speeding up with vertical distance from the floor. However, the overall RMS of the standard deviations is still only 2.1 % indicating that most U/U_{ref} values are close to the mean.

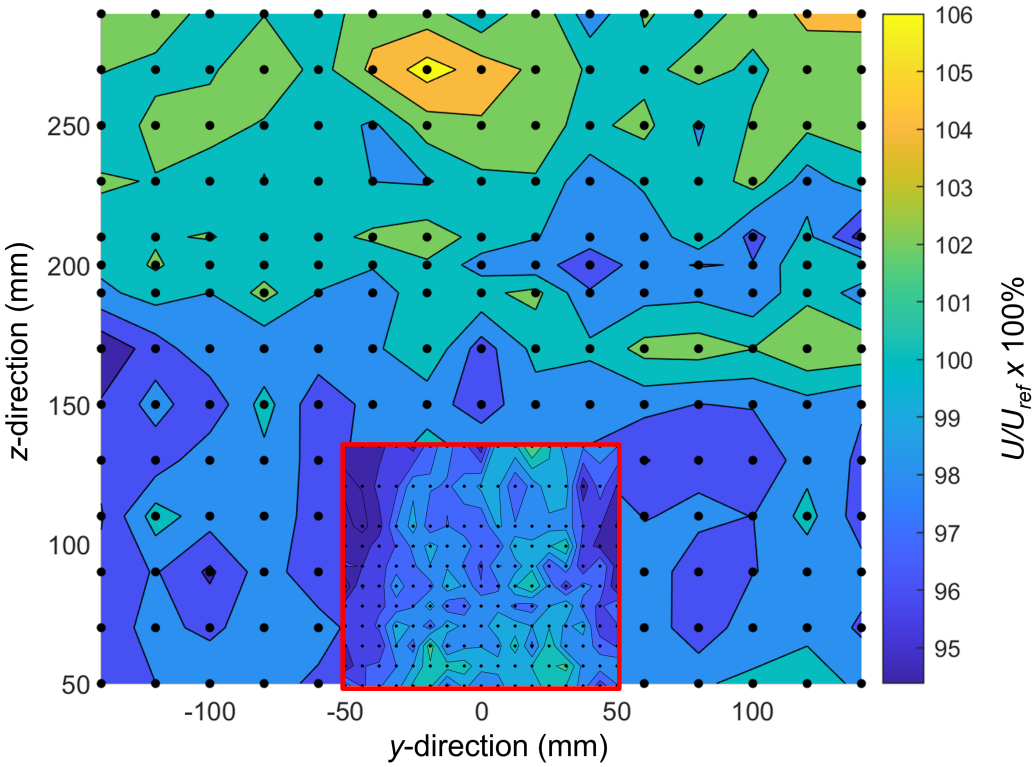

Figure 4.5: Ratio of U velocities to the mean velocity of all of the points in the flow, U_{ref}, for the grid operating in double random mode (4 ± 2 Hz). The red square region denotes the area of the fine mesh scan data points. Measurement taken at 10M.

Measurement locations included planes at 10 and 20 mesh lengths (later referred to as 10M and 20M) away from the grid for the majority of tests. Select test cases were chosen to also have measurements conducted at 30 mesh lengths (30M) away from the grid to view the effects of the turbulence decaying downstream. Each

point was sampled for 180 seconds at 20 kHz and low-pass filtered at 10 kHz on the Dantec Dynamics StreamLine Pro constant temperature anemometer module.

4.3 Traverse

The traverse system that the pitot and x-wire probes were mounted to can be seen in Figure 4.6. The traversing system that the sensors were mounted to utilizes 3 linear traverses with an additional turntable mounted on the carriage of the vertical traverse for a total of 4 degrees of freedom. The traverse system allowed for sensors to be traversed up to 750 mm downstream, 275 mm vertically, and 470 mm in the spanwise direction.

Due to the size and mass of the traverse system, an additional follower traverse was added parallel to the streamwise traverse to stiffen the setup and mitigate any potential vibrations caused by flexibility of the single streamwise traverse. However, the addition of the follower traverse restricted the streamwise movement of the traverse to approximately 750 mm.

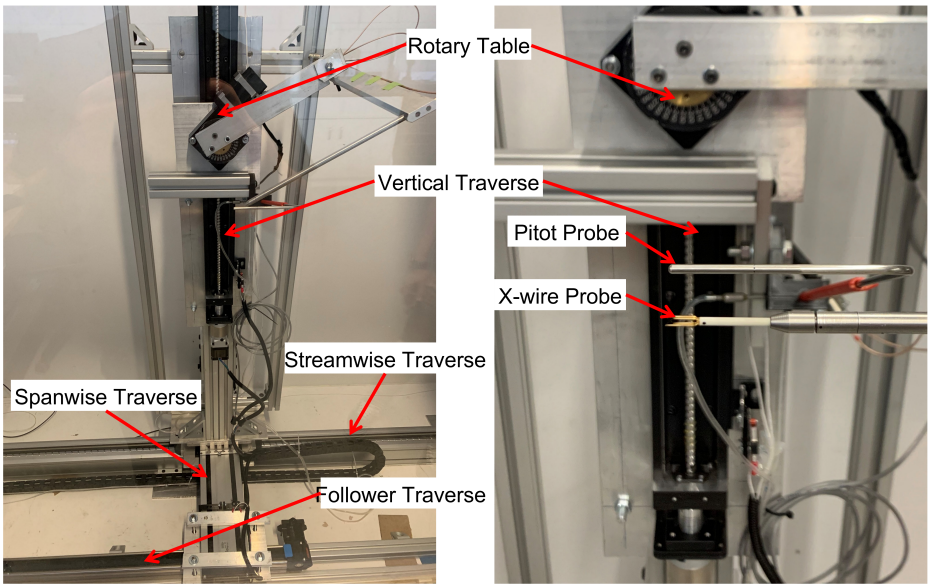

Figure 4.6: (Left) Four degree of freedom traverse system used in this study. (Right) Close-up view of the vertical traverse, rotary table, and the mounted instrumentation.

4.4 Forcing Protocols

Traditionally, active grids have used three main types of forcing protocols: synchronous, random, and double random, as summarized in Section 2.4. In synchronous mode all the rods rotate at the same angular velocity with adjacent rods rotating in opposite directions. In random mode, the magnitude of the angular velocity is kept constant however the direction of rotation changes after a random period of time, referred to as the cruise time. The cruise time is randomly selected from a pre-set range about a mean time for each direction change. Lastly, the double

random mode in which each rod of the grid receives a different random angular velocity magnitude and direction from a given pre-set range and will rotate for the random cruise time. After the cruise time, each rod of the grid is given a new unique random rotational velocity and direction. In this present study, there were two distinct forcing protocols used: the double random mode and oscillations. The double random mode is widely regarded as the mode that produces the most homogeneous isotropic turbulence while producing a spectra that is largely without discernible peaks correlating to the rotational rate [15], unlike in a single random mode. Hearst and Lavoie [18] showed that cruise time does not have much of an effect on the turbulence produced and thus the cruise time for this research was loosely based on the cruise times reported by [18] who used 2.11 ± 2 s and [45] who used 1 ± 0.5 s. The chosen cruise time for this research was fixed at 1.5 ± 1 s. The rotational rate, certainly a much more influential parameter, ranged from 5 ± 2.5 Hz to 16 ± 8 Hz. The mean rotational rates (Ω) were selected to achieve an approximate Rossby number range of 35 to 110 for a flow velocity of $U = 14$ m/s, similar to the higher Rossby numbers reported in literature [18, 45]. To avoid potential mechanical problems with the grid elements coming unglued from the shaft, the mean rotational rate was limited to 16 Hz, though the motors were capable of spinning the assemblies up to a maximum of 33 ± 16.5 Hz which would have driven the Rossby number down to approximately 17 for $U = 14$ m/s and 8.5

for $U = 7$ m/s. The formula for calculating the deviations of the rotational rate from the mean (ω) was calculated as $\omega = \Omega/2$ as used by Larssen and Devenport [45] for the majority of their experiments.

In an effort to reduce the blockage and subsequently the produced turbulence, oscillations were used in which each rod would oscillate at a given amplitude about their fully open position. The three amplitudes that were tested (25°, 45°, and 67.5°) were run at oscillation frequencies ranging from 0.5 to 16 Hz. This gave a Rossby number range of approximately 40 to 1360 for a flow velocity of 17 m/s, a much wider range than what has been reported in literature.

5 Results

The results presented in this chapter concern the observations and conclusions drawn from the active grid experiments outlined in Section 4.4. The nature of this work was explorative in the range of capabilities of the active grid system that was developed, with the overarching goal of comparably simulating aspects of on-road flow conditions. Five main sections follow: the discussion of turbulence intensity, Taylor Reynolds number and spectra, isotropy, turbulence length scale, and lastly the dissipation rate. Each section is preceded by the results of the double random forcing protocol, followed by the results from the oscillations forcing protocol. As mentioned in Section 4.2, presented results have been calculated by sampling 10 points in each streamwise plane for 180 s. The turbulence statistics were calculated for each of the 10 measurement points before being averaged together to yield a single value. An example calculation for the double random case DR7 can be found in Appendix B. The nomenclature used for naming the tests include a DR prefix for the double random cases and an OS prefix for the oscillations cases. The prefix

is followed by a number that follows no particular order. Appendix A includes a summary of the results including the name of each experiment, the corresponding operating parameters, and the results of the experiments.

5.1 Turbulence Intensity

Turbulence intensity is defined as the ratio of fluctuating flow velocity to the mean flow velocity and is often expressed as a percentage to quantify the strength of the fluctuations in the flow. Turbulence intensity generally is a function of the blockage, increasing as the blockage increases. Hearst & Lavoie [18] demonstrated the relationship between turbulence intensity and blockage when they used three different grid element geometries with three different blockages. The grid elements with the highest blockage consistently produced the highest turbulence intensities in Hearst & Lavoie's [18] experiments. The turbulence intensity imparted on the flow by the grid in this thesis in its fully open position is 5.5 % at 10M and 3.3 % at 20M. Hearst & Lavoie [18] measured a turbulence intensity of $T_q = 1.8\%$ at 41M with their grid fully open.

5.1.1 Double Random

The highest turbulence intensities produced in this study were in consequence to the double random forcing protocol. The highest intensity that was recorded measured

33 % at 10M. This case corresponded to a rotational rate of 5 ± 2.5 Hz and a Rossby number of 110. This is in line with values reported by Makita [37] who measured turbulence intensities of up to 37 % at 10M away from their grid. However, there is limited data in this proximity to the grid. The majority of existing research in the literature is taken in the far field [16, 18, 47, 50, 51, 54, 63]. The location of 10M included in the present research was chosen as it corresponds to approximately where the front of a vehicle would be in the test section. Further downstream of the grid at 20M and 30M the turbulence intensity measured 24 % and 20 %, respectively. The lowest turbulence intensity was measured for one case with the nozzle velocity of 6.7 m/s where the rotational rate was 12 ± 6 Hz, producing an intensity of 23 % at 10M and 18.3 % at 20M.

Similar to the relationship between length scale and Rossby number, turbulence intensity is also well correlated with Rossby number. Hearst & Lavoie showed that for their active grid system, the turbulence intensity increased sharply for Ro<50 before asymptotically plateauing for 50<Ro<150 [18] as seen by the black dots in Figure 5.1. Results from the present study are included in Figure 5.1 in terms of TI_q for comparison with Hearst & Lavoie [18]. However, the Rossby number range where the intensity appears to plateau is shifted to the right. The sharp increase in the turbulence intensity for 0<Ro<20 that is seen in the Hearst & Lavoie data, is not shown in the present results, since measurements were not taken at these

lower values of Ro. In addition, Hearst & Lavoie [18] reported their measurements at 41M while the measurements presented in this thesis were limited to 30M due to the length of the streamwise traverse and by the size of the collector at the downstream end of the testing section. However, a theoretical projection of the turbulence intensity at 40M is shown on Figure 5.1 by the light blue band. The theoretical turbulence intensity at 40M was calculated using the energy decay rate equation given below from [52] using a decay exponent of $-n_u = -1.3$ and a virtual origin assumed to be $X_0 = 0$. The projected turbulence intensity at 40M is still higher than that shown by Hearst & Lavoie as they used a biplanar grid which improves different characteristics of the turbulence, one of them being a reduced turbulence intensity.

$$\frac{\langle u' \rangle}{\langle u \rangle} = A_u \left(\frac{X - X_0}{M} \right)^{-n_u}$$

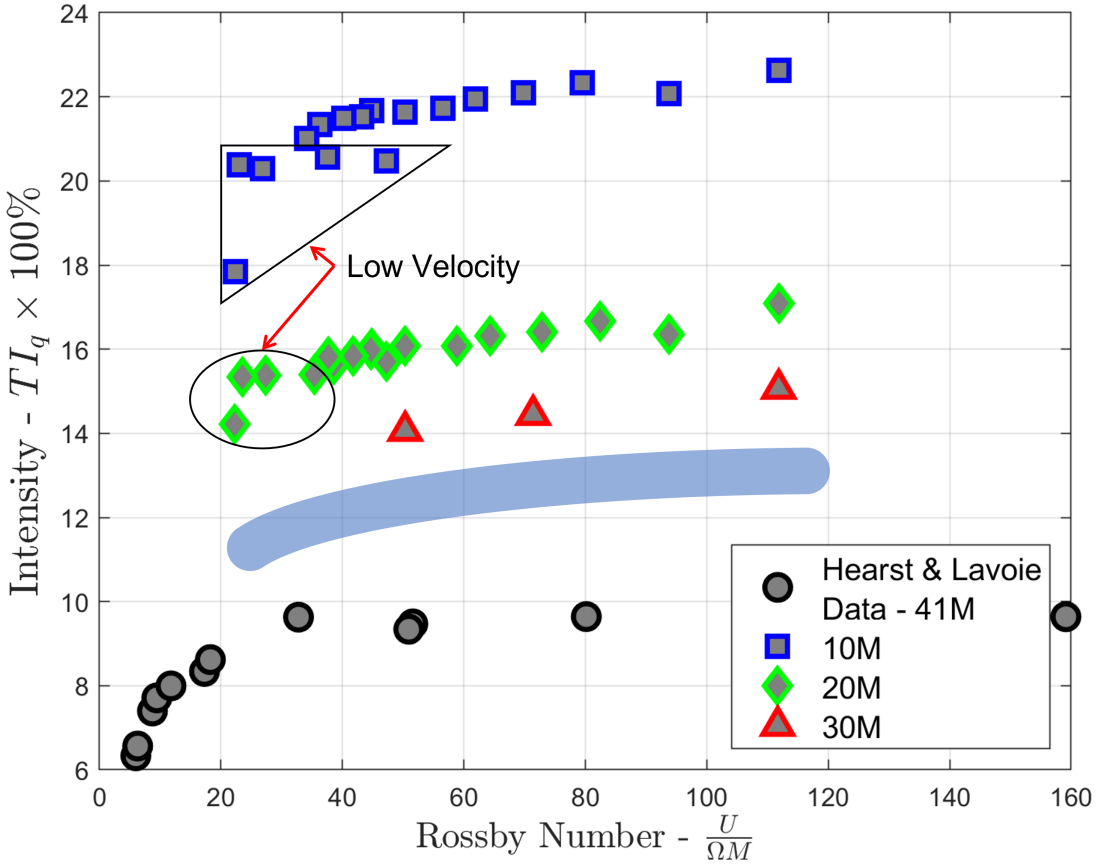

Figure 5.1: The relationship of turbulence intensity with Rossby number for 10M, 20M, and 30M. Also shown is data recreated from [18] for their solid square grid element cases at 41M. Low velocity cases were conducted at velocities between 6.7 and 9.6 m/s. A theoretical projection of the turbulence intensity with Rossby number at 40M is shown by the blue band.

5.1.2 Oscillations

When the grid was operated in the oscillations mode, it would run with a constant oscillation amplitude (25°, 45°, or 67.5°) and oscillation frequency. In oscillations mode, the turbulence intensity became independent of the oscillation rate, remaining at a near constant value for all of the oscillation rates tested. Instead, the turbulence intensity was dependant on the oscillation amplitude, increasing as the amplitude increased. Figure 5.2 shows how the turbulence intensity increases with increasing oscillation amplitude while remaining nearly constant for all oscillation rates. At an oscillation amplitude of 25° the turbulence intensity ranged from 4.6 % to 5 %, which was greater than the baseline fully open grid in passive mode, having a turbulence intensity of 3.3 % at the same downstream location. The oscillation amplitude of 45° produced intensities ranging from 5.7 % to 7.1 %, and 67.5° produced a range from 6.7 % to 9.7 %.

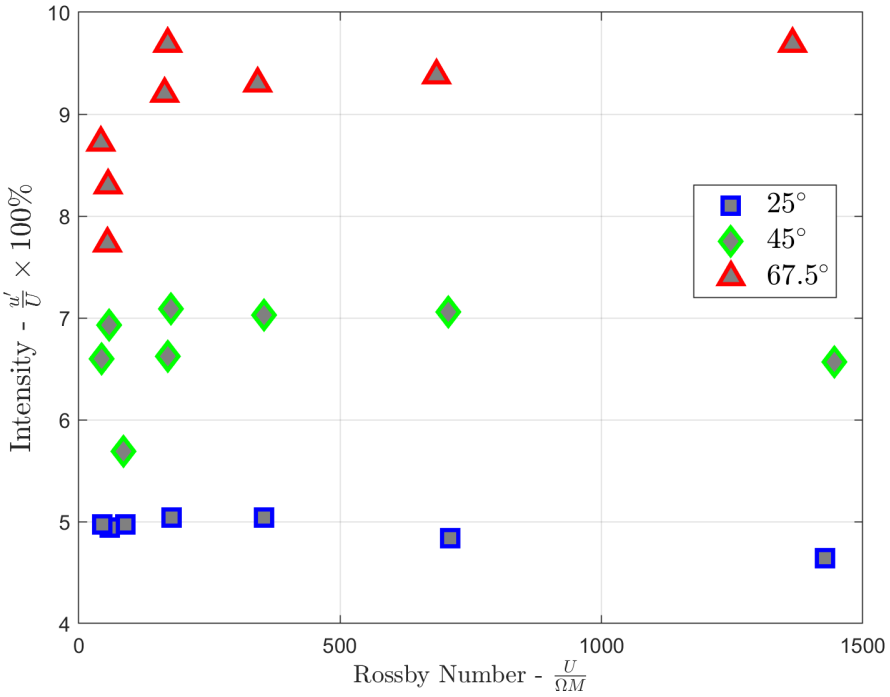

Figure 5.2: The relationship of turbulence intensity with Rossby number for 25°, 45°, and 67.5° oscillation amplitudes. Measurements taken at 20M.

Particularly interesting about the oscillation mode is that the length scales varied widely despite the turbulence intensity remaining similar for each of the oscillation rates for a given amplitude. Figure 5.3 illustrates how the longitudinal length scales were able to be manipulated by as much as two orders of magnitude while keeping the intensity near constant. This behaviour is particularly useful for targeting a specific turbulence intensity while manipulating the size of the turbulence length scales.

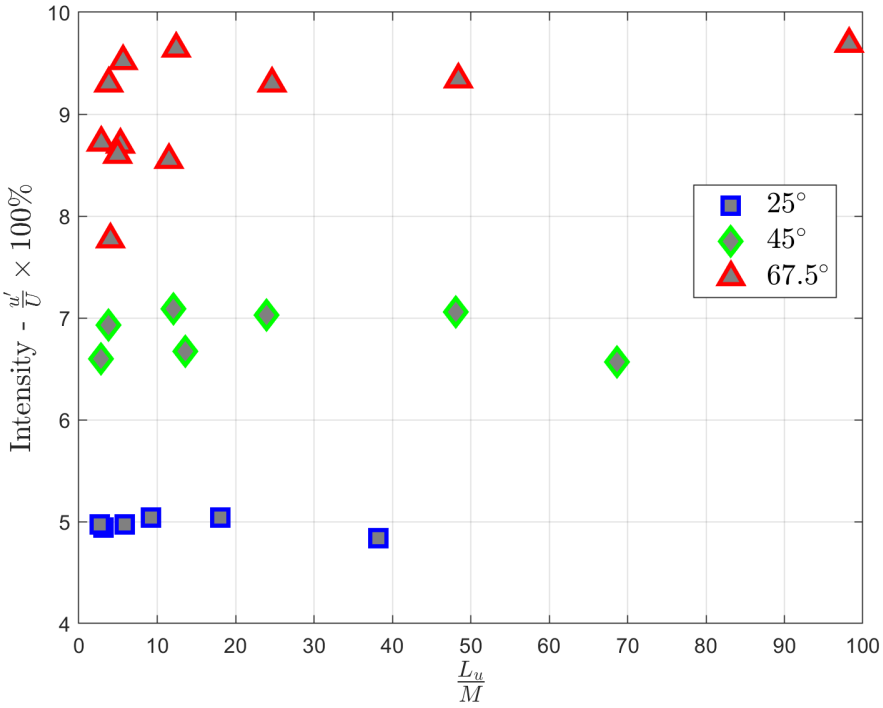

Figure 5.3: The streamwise turbulence intensity shown with respect to the longitudinal length scale. Measurements taken at 20M.

5.2 Taylor Reynolds Number and Spectra

The local Reynolds number that is commonly used in the discussion of turbulent flows is the Taylor Reynolds number $\mathrm{Re}_\lambda = u'\lambda_g/v$ [16, 35, 45, 50]. Generally, as the Taylor Reynolds number of a flow increases, so does the size of the inertial subrange which implies that there is a wider range of scales in the flow [19, 35]. In light of this, the Taylor Reynolds number should be as large as possible since the underlying Kolmogorov theory relies on an infinite Taylor Reynolds number

to achieve a broad spectrum of scales and to produce a well defined -5/3 inertial subrange slope [15, 44]. Typical atmospheric boundary layer measurements yield a Taylor Reynolds number on the order of 10^4, however most laboratory wind tunnel facilities are limited to Taylor Reynolds numbers on the order of 10^3 due to size [44]. Nevertheless, the inertial subrange can still be viewed for $\mathrm{Re}_\lambda > 250$ [37].

Previous active grids have generally been limited to $\mathrm{Re}_\lambda < 1000$. However, some authors have been able to exceed this value [44–46] with Bodenschartz et al. [35] producing a local Reynolds number of $\mathrm{Re}_\lambda = 1620$ in their variable density wind tunnel, some of the highest values produced by an active grid. At 20M, the grid used in this research produced a maximum Reynolds number of $\mathrm{Re}_\lambda = 880$ when operated in the double random mode DR1. For oscillations mode, the OS23 case produced the highest Reynolds number of $\mathrm{Re}_\lambda = 430$ at 20M, approximately half that of the random mode. These relatively high Taylor Reynolds numbers contributed to spectra with well defined inertial subranges with slopes approaching the universal -5/3 slope. The lowest Reynolds number at 20M produced for the double random case was for DR8a which measured $\mathrm{Re}_\lambda = 210$ at a mean flow velocity of 6.7 m/s. For the oscillations mode, the lowest Reynolds number produced was from OS2, measuring just $\mathrm{Re}_\lambda = 110$. However, this case corresponded to the grid operating at an oscillation amplitude of 25° and an oscillation frequency of 0.5 Hz so the solidity of the grid was very low since the grid elements were not making full rotations.

The energy spectra is a more reliable way of ascertaining the distribution of the energy within a turbulent flow over a range of frequencies than length scales or intensities. The premultiplied spectra for two different test cases as well as for the grid held fully open in passive mode can be seen in Figure 5.4. The spectra in Figure 5.4 have been premultiplied by the wave number so that the total energy content is represented by the area under the curves. The two test cases shown in Figure 5.4 were from the double random mode where DR1 was run at 5 ± 2.5 Hz with a flow velocity of approximately 14 m/s while the DR2a case was run at 6 ± 3 Hz with a flow velocity of approximately 7 m/s. The two different spectra are plotted to illustrate differences observed for different Taylor Reynolds numbers. DR2a had a Reynolds number of $\mathrm{Re}_\lambda = 230$ which was sufficient to produce a decently well defined inertial subrange. However, DR1 produced a Reynolds number that was almost 4 times larger than that of DR2a at $\mathrm{Re}_\lambda = 860$ which shifted the entire spectra up by almost an order of magnitude. This also had the effect of producing an inertial subrange that was wider that the DR2a case. Both test cases however produced far greater Reynolds numbers than with the grid statically open. With the grid fully open in passive mode, the produced Taylor Reynolds number of $\mathrm{Re}_\lambda = 70$ was insufficient to produce a spectra with a wide inertial subrange. The rather low $\mathrm{Re}_\lambda = 70$ is on the order of what a traditional passive grid would produce.

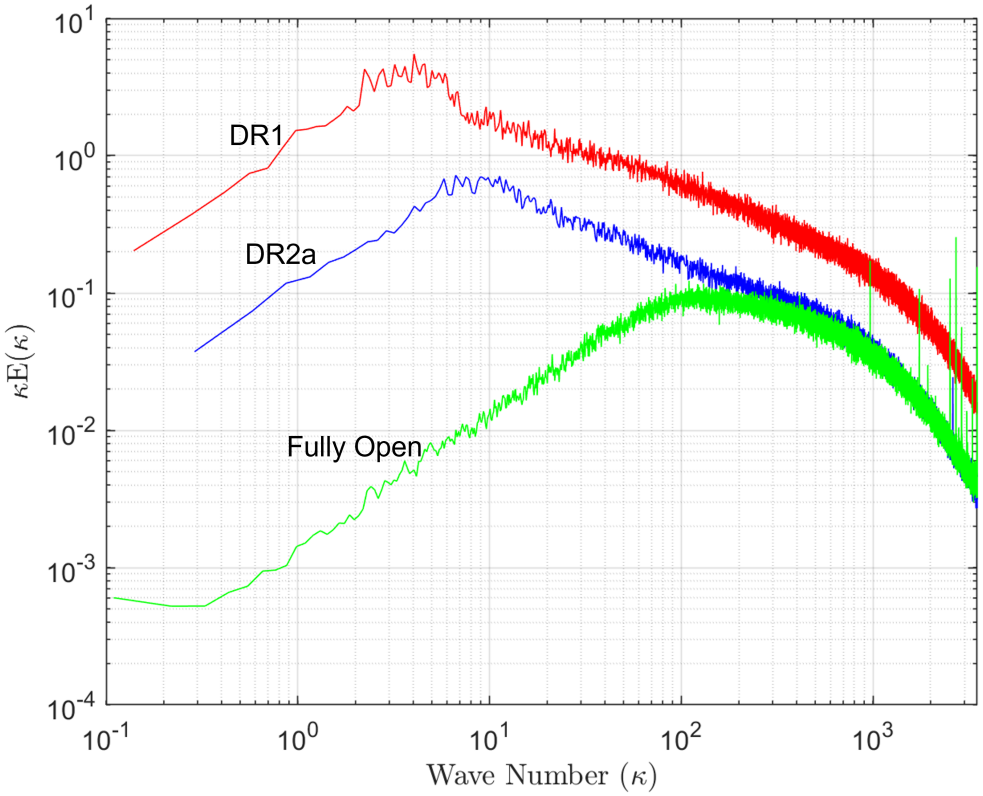

Figure 5.4: The premultiplied spectra of u'/U for the three cases, static, DR1, and DR2a premultiplied by the wave number. Measurements taken at 20M.

The premultiplied spectra for two oscillation cases is shown in Figure 5.5. The case, OS22, shows a typical spectrum for the turbulence produced by the oscillation protocol. The first large peak at $\kappa \approx 6$ m^{-1} corresponds to the oscillation frequency while the rest of the peaks correspond to the harmonics of that frequency. These peaks are similar to the peaks seen in the spectra of an active grid run in a synchronous and single random modes [15]. Here OS22 operated with an oscillation

amplitude of 67.5°, an oscillation frequency of 16 Hz, and a mean flow velocity of 16.9 m/s. In an effort to reduce the magnitude of these peaks and to fill out the spectrum, the vertical rods were set to rotate with a double random mode with 10 ± 5 Hz while the horizontals continued to oscillate at 16 Hz. The result of this can be seen in Figure 5.5 as OS25. However, having the oscillation frequency vary with time, similar to how the rotational rates varied with time in double random mode, would have also likely reduced or eliminated the peaks in the spectrum. The addition of the double random motion increased the Reynolds number slightly to $\mathrm{Re}_\lambda = 380$ from $\mathrm{Re}_\lambda = 260$ that the OS22 forcing protocol produced, which helped to expand the inertial subrange of the spectrum. Furthermore, the double random motion reduced the magnitude of the peaks caused by the oscillations, as well as eliminated much of the harmonics.

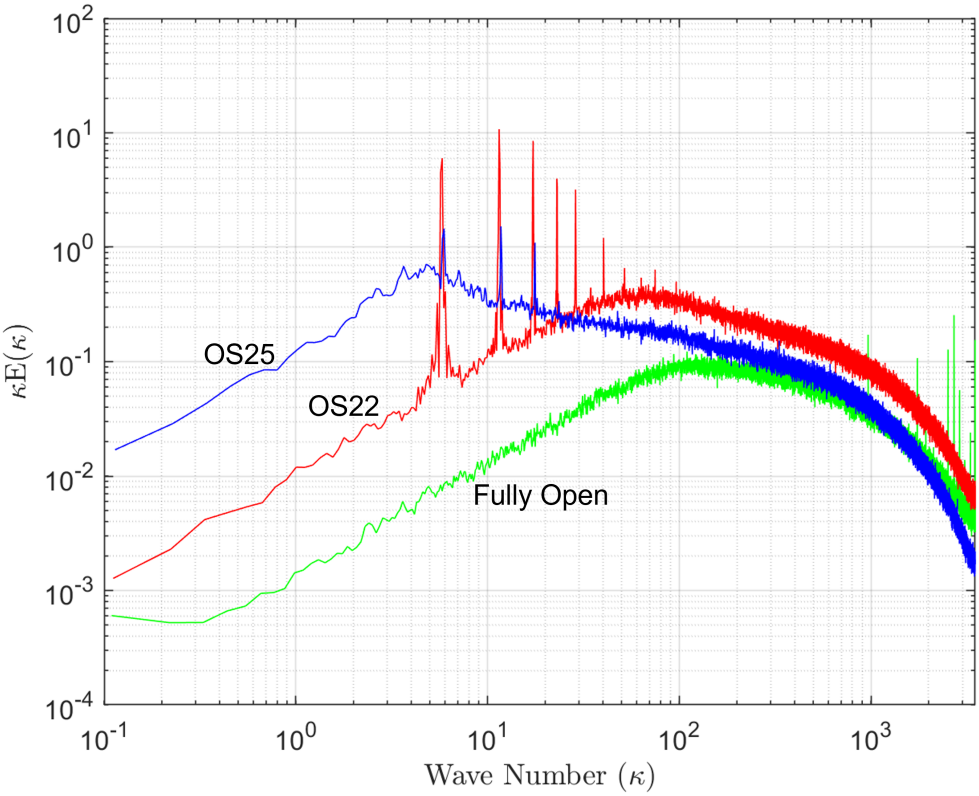

Figure 5.5: The premultiplied spectra produced for two oscillations cases, OS22 and OS25, as well as for the grid fully open. Measurements taken at 20M.

The previous results focused on the comparison of results to those obtained from other active grid systems. However, the main objective of the active grid is to recreate on-road turbulent conditions in an automotive wind tunnel. Results from select present cases are plotted with data recreated from [8] in Figure 5.6. The dashed lines in Figure 5.6 represent the on-road measurements that [8] did

as part of their research. To be able to compare the on-road spectra with the different turbulence generation systems, the reduced frequency and normalized energy spectra $E(f_r)$ have been used [27]. The reduced frequency is given by $f_r = fL_{ref}/U_{ref}$ where L_{ref} for the data collected in this research is 0.1 m, since the wind tunnel is a 1/10th scale model. In the data recreated from [8], L_{ref} is taken to be 1 m. U_{ref} is the mean streamwise flow velocity. The normalized spectra is given by $E(f_r) = E(f)/L_{ref}U_{ref}$. From Figure 5.6 we can see that DR7 case corresponding to 11 ± 5.5 Hz produces significantly more low-frequency energy than the wake from a heavy duty vehicle while the OS25 case almost follows the spectrum of the "dense traffic" quite well. However, the OS25 spectrum appears to have a shallower inertial subrange slope than -5/3.

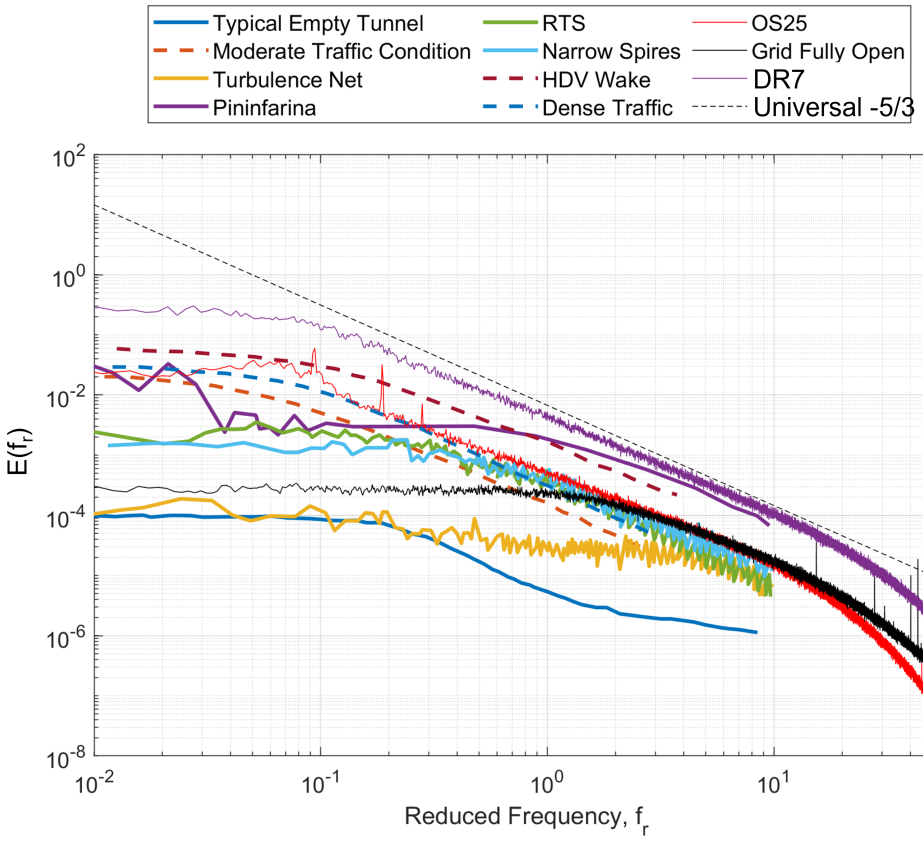

Figure 5.6: Spectra of OS25, DR7, and the grid fully open plotted against data recreated from [8] compiled from various authors as explained by [8].

5.3 Isotropy

The anisotropic ratio is the ratio of the RMS of the fluctuations in the streamwise and spanwise directions $I = u'/v'$. A flow is said to be isotropic if this ratio is approximately unity and anisotropic otherwise. With the grid fully open, the grid produces a flow with anisotropic ratios similar to that produced by a passive grid. At 10M the grid produced an anisotropic ratio of 1.4 and while at 20M an

anisotropic ratio of 1.23 was produced. Vita et al. [64] reported anisotropic ratios of 1.14, 1.19, and 1.2 at 10M for three of their passive grids.

5.3.1 Double Random Mode

In double random mode, at a streamwise location of 10M, the flow is the least isotropic with an anisotropic ratio of approximately 2.00, reaching as high as 2.23 in one case. Generally, active grids with faster rotations show a decrease in the anisotropy [18, 34, 43, 45, 49]. The active grid used in this research consistently shows a decrease in the anisotropic ratio for each of the downstream planes measured as seen in Figure 5.7. Also shown in this Figure are data recreated from [18, 43, 49]. In addition, for the same rotational rate, measuring further downstream at 20M and 30M also improved the anisotropy of the flow by approximately 12 - 13 % at 20M and a further 10 % improvement at 30M. This behaviour was also observed in the values reported by Makita and Sassa [43]. Again, the trend of the anisotropy improving with faster rotations can be observed in both the 20M and 30M planes, achieving an isotropic ratio of 1.7 at a mean rotational rate of 16 Hz for the 20M plane. Lower flow velocities also helped improve the anisotropy of the flow. The slower velocity test cases, shown by the open markers, consistently gave lower anisotropic values than for the higher velocities, achieving an anisotropic ratio as low as 1.56 at 20M for a velocity of $U \approx 7$ m/s. Poorte and Biesheuvel [49] were able to produce near unity anisotropic values at a flow velocity of 0.3 m/s in their water tunnel. Clearly seen in the Figure are much lower anisotropic ratios for Hearst & Lavoie's data than the ratios reported in this thesis. Some reasons for this include that Hearst & Lavoie took their measurements further downstream at 41M allowing the turbulence more time to mix and their grid utilized a biplanar design where the grid elements adjacent to one another of the active grid are installed staggered in two planes. This

method has been shown to reduce the anisotropic ratio down to approximately 1.10 but at the expense of a lower Taylor Reynolds number [18, 45, 49].

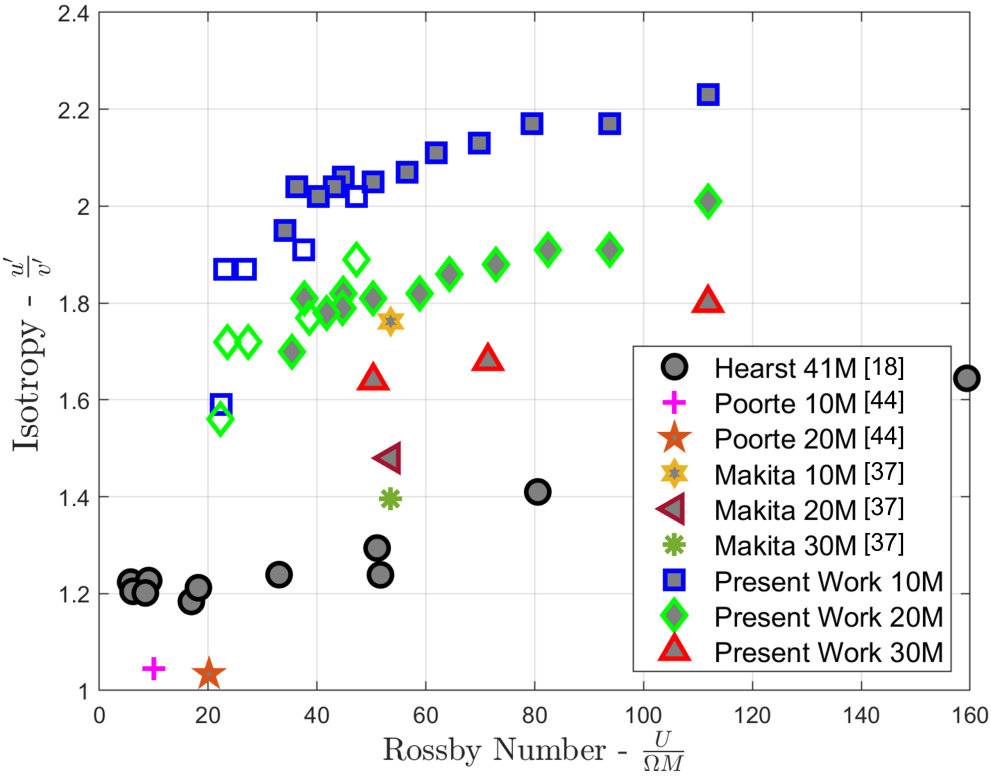

Figure 5.7: Variation of the isotropy with the Rossby number at three different distances from the grid, X = 10 M, 20 M and 30 M. Open markers denote lower velocity cases of $\approx$ 7 - 9.5 m/s. Also shown is data recreated from [18] for their solid square elements and [43, 49].

5.3.2 Oscillations

Figure 5.8 shows the effect of Rossby number on the anisotropic ratio for the three different oscillation amplitudes at three different distances from the grid, $X = 10$M, 20M and 30M. At 10M, the anisotropic ratio does not appear to change significantly with faster oscillations. Increasing the oscillation amplitude from 25 degrees to 67.5 degrees saw an increase from 1.3 to 1.7 in the most extreme cases. Interestingly, the smallest amplitude 25 degrees saw a slight improvement across most cases in the anisotropy when compared to the baseline case with the grid statically open. Further downstream at 20M, the same trend was also observed with the anisotropic ratio increasing with increasing oscillation amplitude as seen in Figure 5.8. However, increasing the oscillation rate showed a noticeable improvement in the anisotropy for all three oscillation amplitudes. Lower Rossby numbers would need to be investigated to confirm how the flow behaves when Ro$<$40 as it appears that the anisotropic ratio is decreasing sharply at low Rossby numbers.

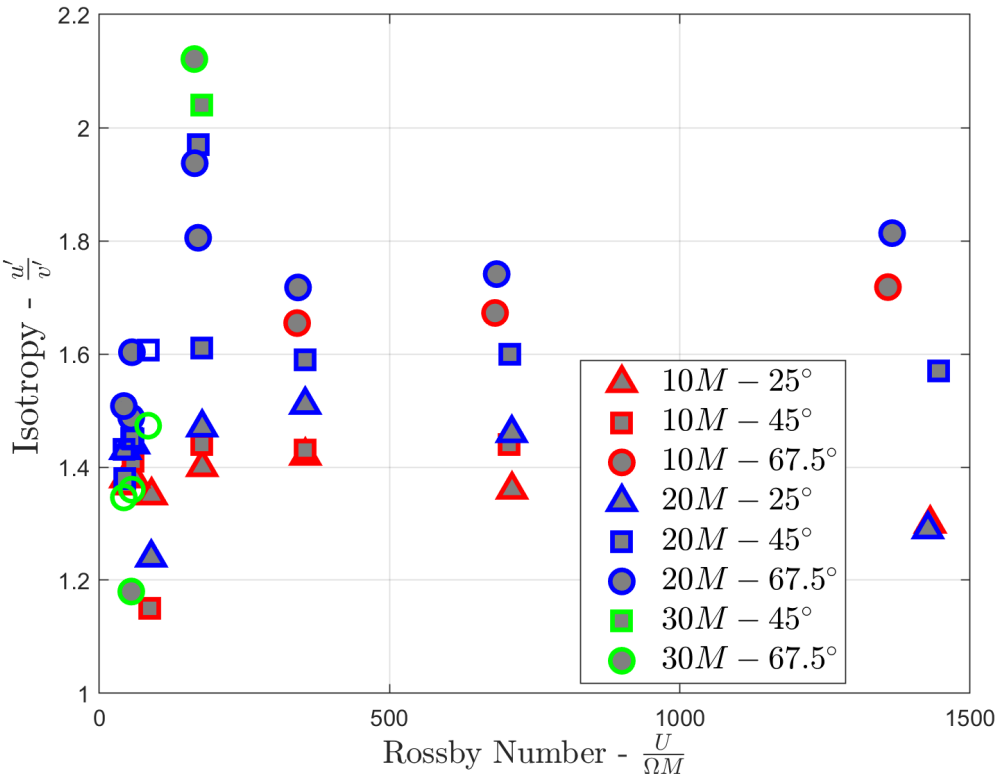

Figure 5.8: The effect Rossby number on the anisotropic ratio for the 25°, 45°, and 67.5° oscillation amplitudes at three different distances from the grid, X = 10M, 20M and 30M. Open markers denote cases where the vertical shafts operated in double random mode.

For the same oscillation rate and amplitude, the anisotropic ratio increased with increasing distance from the grid for most cases, the opposite of the behaviour that is observed in the double random modes.

5.4 Integral Length Scales

The integral turbulence length scale is a method used to characterise the largest energy containing scales in the flow. One of the most common methods employed by researchers to calculate the integral length scale of a turbulent flow is by taking the autocorrelation of the velocity fluctuations signal and integrating it to its first zero crossing, as explained in Section 2.1. In this thesis, the signal was integrated from 0 and the time such that the correlation reduced to 0.1 as some signals had some low frequency oscillations that would significantly increase the time it took for the signal to become decorrelated – artificially inflating the integral length scale. However, this was also particularly a problem for the lower oscillation frequencies (0.5 Hz) of the oscillations forcing protocol. An example of the autocorrelation plot for an oscillations case, OS2, with an oscillation frequency and amplitude of 0.5 Hz and 22.5° respectively, is shown by the red line in Figure 5.9 showing the delayed decorrelation to $\rho(t_*) = 0.1$ ($t_* \approx 0.23$ s). This is contrasted by the blue line of Figure 5.9 showing the autocorrelation for a double random case, DR7, where the signal decorrelates to 0.1 rapidly ($t_* \approx 0.025$ s), almost an order of magnitude sooner.

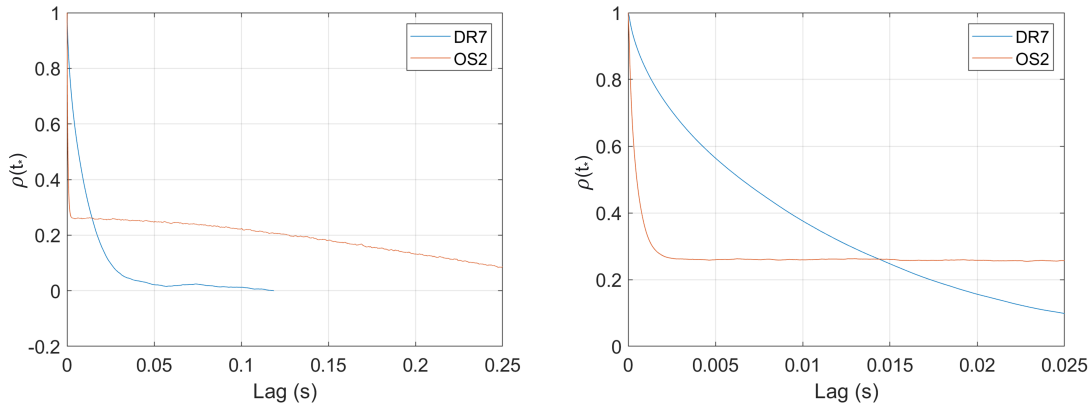

Figure 5.9: Autocorrelation plot for the DR7 double random case and the OS2 oscillations case (left) as well as the same autocorrelation plot zoomed in (right).

Another common method used to calculate the turbulence length scale is to take the inverse of the peak wave number from the premultiplied spectra [63]. Figure 5.10 shows the spectra for the double random mode measured at 10M and 20M calculated using both the integral length scale method and the peak wave number method. The blue markers indicate points that were calculated using the integral length scale method while the red markers indicate points that were calculated using the peak wave number method. Generally the calculated length scales show similar trends, however the trend of the peak wave number method has a steeper slope and produces higher length scale values. For the values reported in this thesis, the integral length scale method was used.

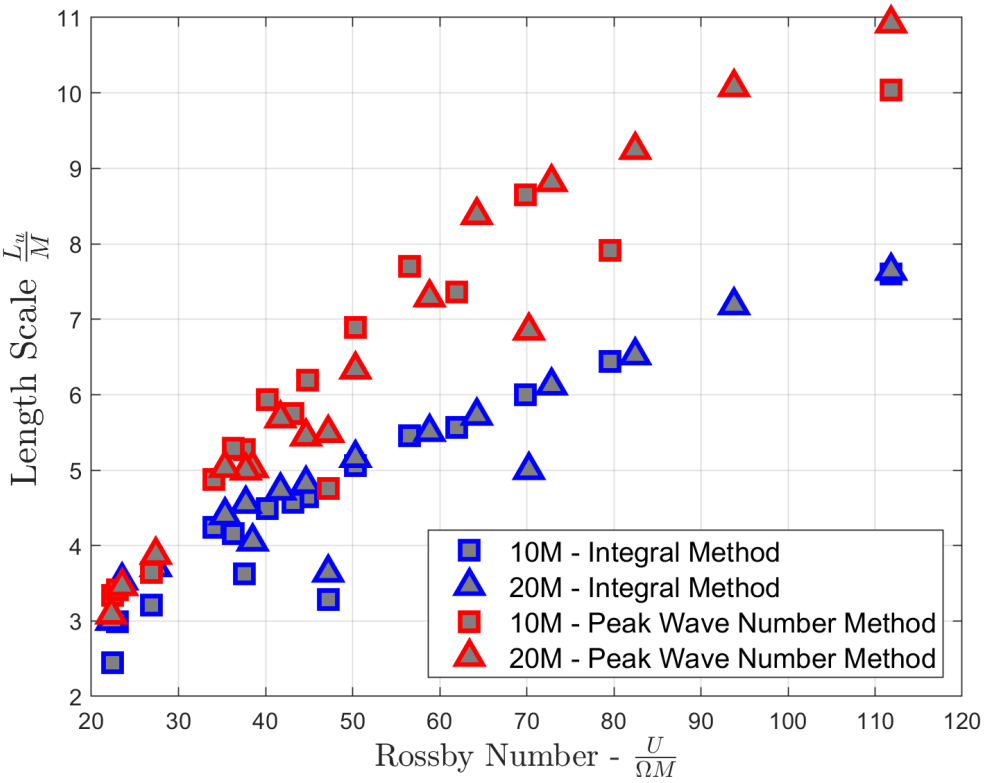

Figure 5.10: The turbulence length scale for the double random mode calculated using the integral length scale method shown by the blue markers, and the inverse of the peak wave number shown by the red markers at 10M and 20M.

5.4.1 Double Random Mode

It was observed that the integral length scales increased with increasing Rossby number (i.e. slower rotations of the grid or higher flow velocity through the grid). This trend is seen in Figure 5.11 where the longitudinal integral length scale, non-dimensionalized by the mesh length, is plotted against Rossby number for three

streamwise locations. Also plotted in Figure 5.11 is data recreated from [18] and [45] depicting the same trend of length scales growing almost linearly with increasing Rossby number.

Noticeably the slope of L_u/M versus $U/\Omega M$ for both Larssen & Devenport and Hearst & Lavoie appears to be shallower than for the values reported in this research. Both of these authors used biplanar grids which reduces the Taylor Reynolds number by a factor of 2 [45], significantly contributing to the smaller length scales for a given Rossby number. For example, for Ro $\approx$ 100 Hearst & Lavoie reported a $\mathrm{Re}_\lambda = 346$ while the author of this thesis reported a $\mathrm{Re}_\lambda = 850$. In addition, both authors were using closed jet test section wind tunnels rather than the 3/4 open-jet wind tunnel used in this research which perhaps bounded the size of the length scales [58].

At 20M downstream, the largest integral length scales that were produced measured 0.19 m at $\mathrm{Re}_\lambda = 860$, almost a magnitude larger than the mesh size, when the grid was operated at a mean rotational rate of 5 Hz. The smallest integral length scale measured 0.075 m at $\mathrm{Re}_\lambda = 210$ when the grid operated at a mean rotational rate of 12 Hz.

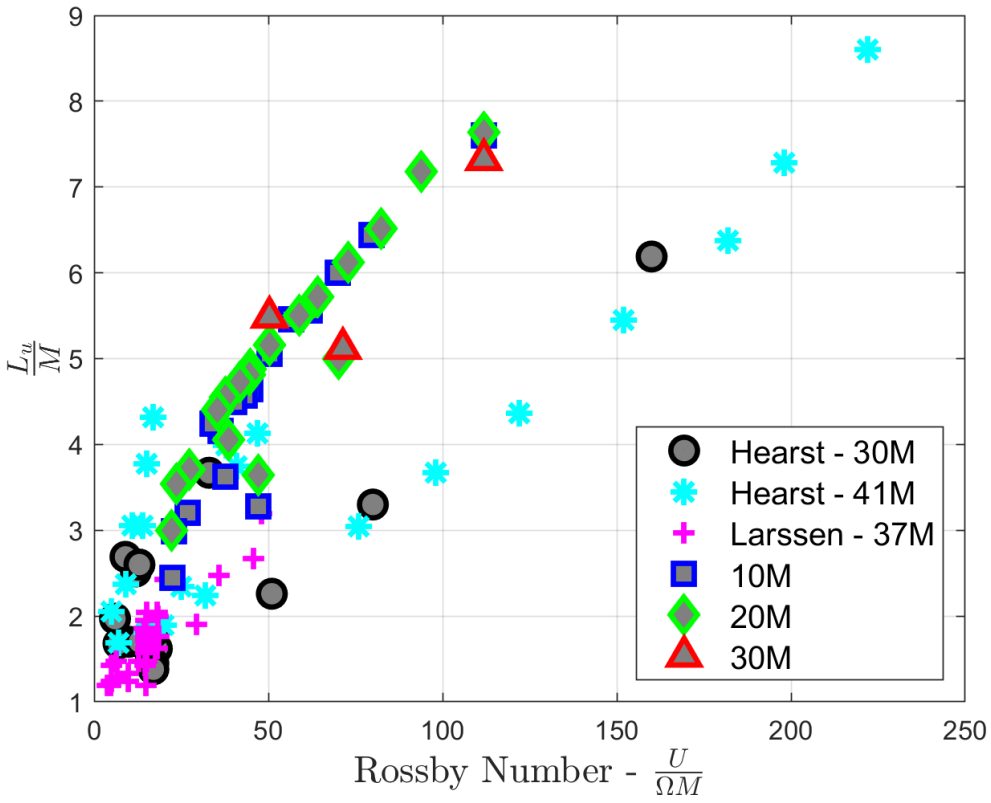

Figure 5.11: The turbulence length scale linearly increasing with Rossby for different streamwise locations. Also shown is data recreated from [18] and [45].

5.4.2 Oscillations

The autocorrelation method used to calculate the integral length scales was found to be unsuitable to calculate an appropriate length scale for the 22.5° oscillation amplitude cases with an oscillation frequency of 0.5 and 1 Hz as the signal did not decorrelate to 0.1 for a long time as shown above in the left image of Figure 5.9.

The resulting length scales for these cases were unreasonably large, suggesting that the length scales were larger than the wind tunnel itself. For this reason, the length scales for the 0.5 and 1 Hz oscillation cases have been omitted.

The oscillations protocol was very useful in reducing the overall blockage of the system while allowing for relatively long streamwise length scales to be produced but with lower intensity values that were more in-line with the target metrics laid out in Table 2.1 from Section 2.2. Operating an active grid with oscillations has not been used to produce low intensity homogeneous isotropic turbulence to the knowledge of the author. However, shear turbulence has been produced through oscillations where the amplitude of the oscillations increased with vertical height of the grid [16, 54]. It was observed that L_u/M exhibited the same linear behaviour with Rossby number that the double random mode produced as seen in Figure 5.12. As the oscillation amplitude increased from 25° through 67.5°, the slope of L_u/M versus Ro became shallower indicating that the size of the length scales decreases with larger oscillation amplitudes. This is the behaviour that would be expected as the blockage of the grid increases and the grid "chops" more of the large length scales with each oscillation.

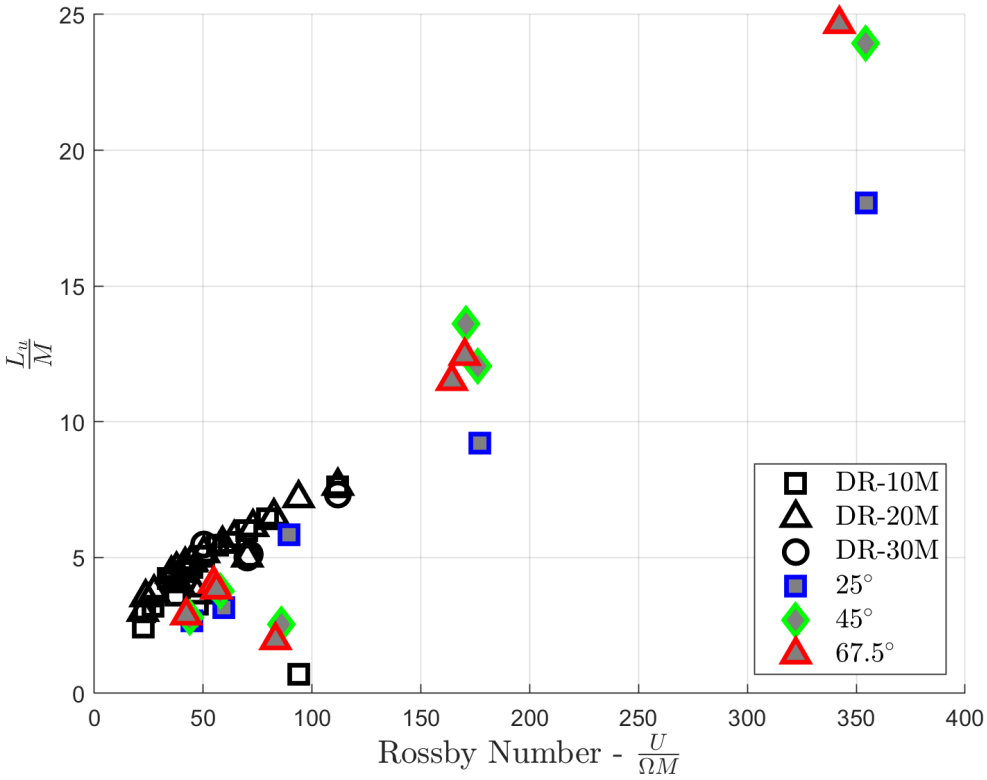

Figure 5.12: The relationship between Rossby number and the turbulence length scale for the different oscillation amplitudes at 20M. Also included are the double random cases for 10M, 20M, and 30M shown in black.

Much like the relationship between Rossby number and turbulence length scale for the double random protocol, slower oscillation speeds consistently produce the largest length scales. The largest scale was produced at an oscillation speed and amplitude of 0.5 Hz and 67.5° measuring approximately 2.46 m which is on the order of the size of the testing section. It is hypothesized that since the rods of

the grid were synchronized with adjacent rods oscillating opposite to each other, that the grid was acting as a gusting system. Evidence of these gusts can be seen in Figure 5.13 which shows the 10 Hz low-pass filtered streamwise velocity time response for the OS16 case which used an oscillation frequency and amplitude of 0.5 Hz and 67.5° respectively. A clear periodic trend in the velocity signal can be seen with a period corresponding to the oscillation frequency of 0.5 Hz. The OS16 velocity signal is contrasted by the double random streamwise velocity response signal, DR7, which has also been low-pass filtered at 10 Hz to make the trends easier to see. The DR7 signal does not exhibit the same sort of periodic trend and is instead much more chaotic and random. To mitigate the gusting effect, the oscillations should utilize an element of randomness. This same gusting was not observed in the faster oscillation frequencies. The smallest length scale of 0.06 m was produced by oscillating the shafts with an amplitude and frequency of 45° and 16 Hz respectively.

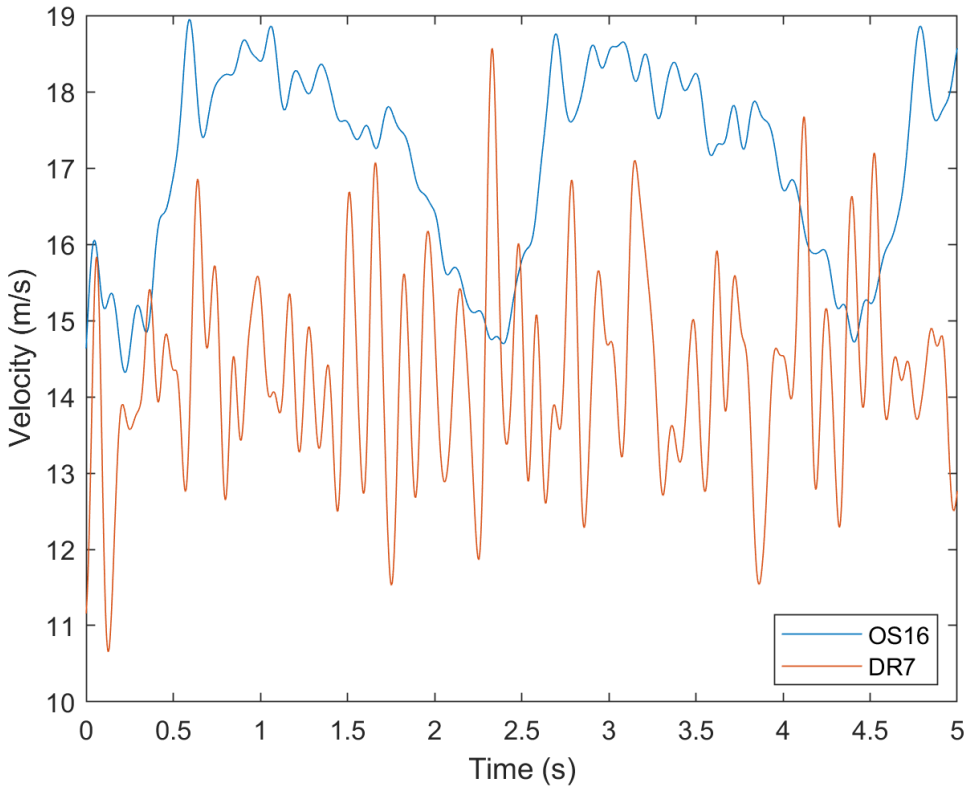

Figure 5.13: Time series of the velocity signal for OS16 and DR7 showing the gusting behaviour of the system operating at low oscillation frequencies versus the random behaviour of the DR7 signal. Data has been low-pass filtered at 10 Hz.

A limited number of cases had the vertical shafts operating in a double random mode at 10 ± 5 Hz while the horizontal shafts operated in the oscillations mode. It was found that for a given oscillation frequency, the size of the large length scales could be nearly doubled while maintaining a near constant turbulence intensity by having the vertical shafts operate in double random mode while the horizontals

operated in oscillations mode. For example, OS22 had an oscillation frequency and amplitude of 16 Hz and 67.5°, and produced a length scale and intensity of 0.07 m and 8.7 % respectively. However, OS25 which had its vertical shafts operating in double random mode at 10 ± 5 Hz and its horizontal shafts operating in oscillation mode at 16 Hz and 67.5° amplitude, produced a length scale and intensity of 0.12 m and 8.6 % respectively – an increase of 71 % in the size of the length scale while maintaining a similar turbulence intensity.

Figure 5.14 shows how the length scale and intensity data collected at 20M in this thesis compares to on-road measurements made by [13]. It is clear that the intensities produced by the double random forcing protocol were too high to match on-road measurements and the produced length scales were too small. In contrast, the oscillations forcing protocol produced turbulence intensities and length scales that were in the approximate range of the on-road measurements by [13].

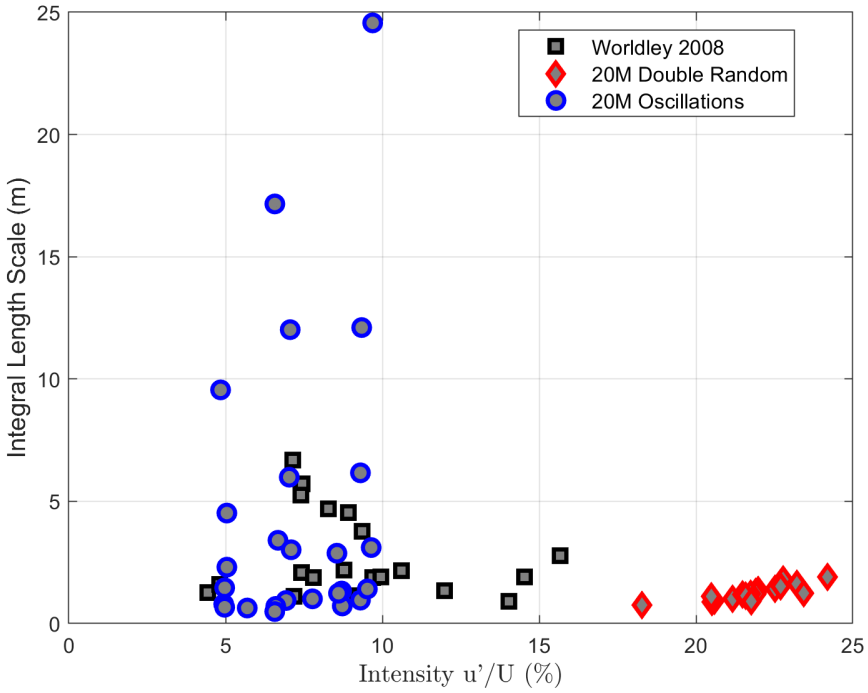

Figure 5.14: The integral length scale versus turbulence intensity for the double random and oscillations forcing protocols at 20M. Data has been scaled to full scale. Also shown is data from [13] for their on-road traffic measurements.

5.5 Dissipation Rate

Lewis Richardson Fry first proposed the idea of the energy cascade in 1922 [36]. Fry noted that turbulence is composed of eddies of different sizes and that turbulence first enters a flow at its largest size characterized by the length scale L_u [65]. However, Fry also noted that these large scales are inherently unstable, and thus collapse into smaller and smaller eddies, transferring their energy in the process

[65] until viscous forces dissipate the remaining energy as heat. The rate at which energy is dissipated is known as the dissipation rate, which is also equal to the energy that is cascaded down to the smallest scales [19]. The dissipation rate, assuming local isotropy, is given by:

$$\epsilon = 15v\overline{\left(\frac{\partial u}{\partial x}\right)^2}$$

where $\partial u/\partial x$ is the streamwise derivative of the longitudinal velocity fluctuations [47]. This is the equation used herein to calculate the total dissipation rate for each of the operating parameters. However, some authors find it more convenient to discuss the dissipation rate in terms of its nondimensionalized dissipation rate constant given by $C_\epsilon = \epsilon L_u/u'^3$, which is independent of Re_λ when it is sufficiently high [36]. This equation works on the assumption that the rate of energy supplied by the large scales is equal to the rate of dissipation in the small scales [63]. This is because u'^2 is proportional to the kinetic energy per unit mass of the large scale turbulence and u'/L_u is proportional to the rate of energy transfer [36] in the equation $\epsilon \approx u'^3/L_u$.

Tennekes and Lumley [66] provide an alternative method of calculating C_ϵ without the need to calculate ϵ first by $C_\epsilon = 15\mathrm{Re}_{Lu}/\mathrm{Re}_\lambda^2$ where Re_{Lu} is the Reynolds number based on the integral length scale. It was found that this method produced C_ϵ values that were approximately 7 % lower for the oscillations forcing

protocol, and 22 % lower for the double random forcing protocol. The former method is the method used to calculate the C_ϵ in this thesis.

5.5.1 Double Random Mode

In contrast to the results obtained by Mora et al. [67] where their measured C_ϵ remained mostly constant with Re_λ, the results obtained in this thesis show that when $\mathrm{Re}_\lambda < 500$, C_ϵ appears to experience exponential decay, only becoming approximately constant when $\mathrm{Re}_\lambda > 600$. Similar decay behaviour can be seen in the data from Puga and LaRue [63] recreated in Figure 5.16, however the range where their data sees the exponential decay appears to be shifted to the left. The shift in the data is potentially due to the much lower turbulence intensities measured by Puga and LaRue (≤ 11 %), contributing to a lower Re_λ, as well as the location where their measurements were made were much further at 45 - 142M. Vassilicos claims that C_ϵ may asymptote to different values depending on the inlet boundary conditions [68]. Puga and LaRue [63] show that their the data did reach a constant of $C_\epsilon = 0.65$ at $\mathrm{Re}_\lambda > 500$. The C_ϵ for the double random had a large spread at $\mathrm{Re}_\lambda > 600$, however, the data does appear to be bounded as seen in Figure 5.16. Much lower values of $C_\epsilon \approx 0.2$ were reported by [36] however they also reached a constant value sooner at $\mathrm{Re}_\lambda > 200$. It has been suggested that there is no universal value of C_ϵ at high Re_λ values [69].

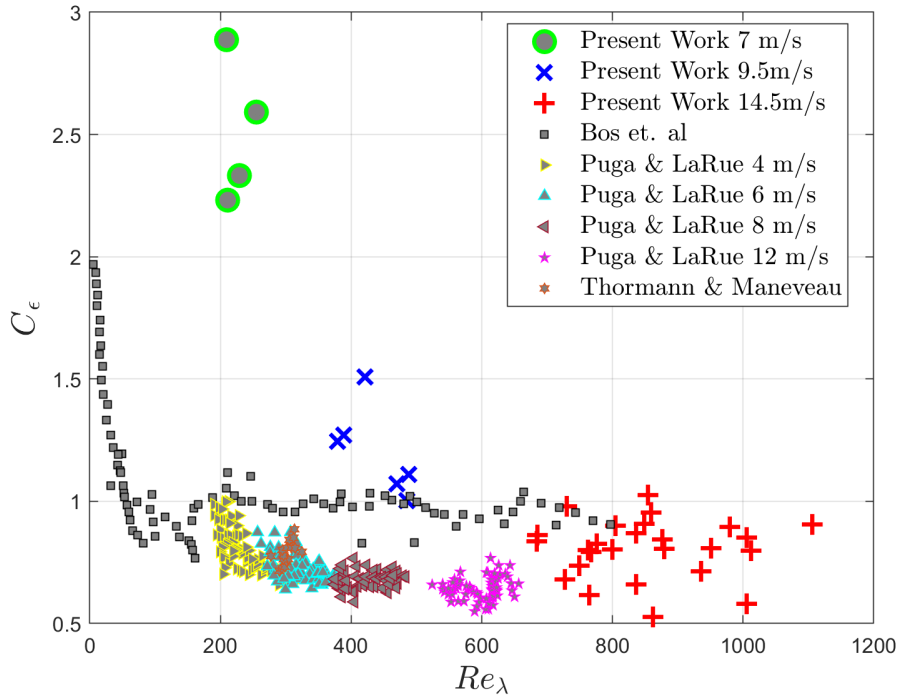

Figure 5.15: The energy dissipation constant C_ϵ (from 10M, 20M, and 30M) varies with Re_λ for different flow velocities with the grid operating in the double random mode. Also seen is data recreated from [52, 63, 69].

5.5.2 Oscillations

The strong trend of C_ϵ decreasing to a constant value for a sufficiently high Re_λ that was shown for the double random protocol was not similarly shown for the oscillation protocol. Figure 5.16 shows the lack of a trend for C_ϵ with Re_λ even for higher values of Re_λ. Figure 5.16 includes data from the oscillations protocol with the lower oscillation frequencies (0.5 and 1 Hz) removed as it was shown earlier

that the estimate for the integral length scale for these cases was skewed. Also seen in the figure is the data from Figure 5.16 plotted in black to show how the data obtained from the oscillations protocol compares to that of the double random protocol.

The values of C_ϵ are also much higher than what would typically be expected. This is likely due to the much larger length scales caused by the oscillations system acting like a gusting system. In addition, the significantly lower intensities also contribute to a higher C_ϵ. More investigation with oscillation protocol will be needed to verify if and at what Re_λ the C_ϵ converges to a constant value.

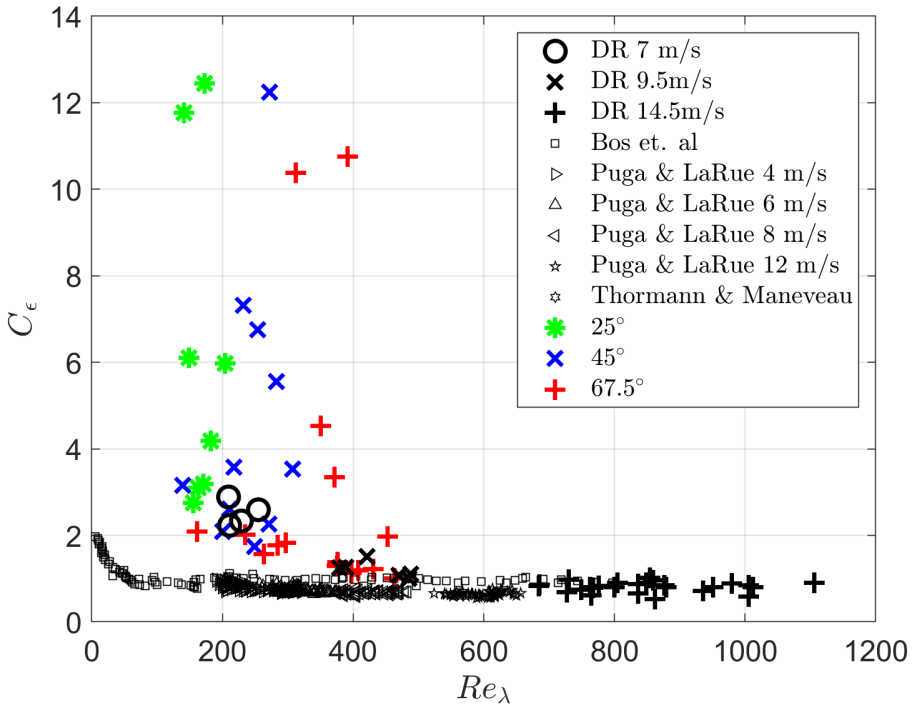

Figure 5.16: The relationship of C_ϵ with Re_λ for three different oscillation amplitudes with the low oscillation frequency cases removed. Also plotted is the data from Figure 5.16.

6 Conclusions

The design and performance of an active grid that operates as a broadband turbulence generation subsystem was explored. The active grid was part of a novel system having three subsystems targeting broadband turbulence, unsteady flow, and yaw. The results pertaining to the active grid subsystem were the focus of this thesis.

Unique to the active grid subsystem, was the design of the grid elements themselves. The main grid elements were designed to produce relatively low drag in the fully open position and a relatively high drag as the angle of attack of the grid element increased in comparison to a baseline squared and a rounded geometry, respectively.

Measurements of the flow produced by the active grid subsystem were performed at three downstream locations of $X/M = 10$, 20 and 30. The nearest-to-grid location represented the approximate location of the front edge of a vehicle in this type of wind tunnel, whereas the other locations were nearer to the downstream end of a vehicle and in the vehicle wake. The flow measurements made using thermal anemometry were used to determine the flow uniformity, turbulence intensity,

turbulence lengths scales, energy distribution and dissipation. The active grid was operated over a range of non-dimensional Rossby numbers in a double random mode, as well as in oscillations.

It was shown that in the near proximity of the grid, the flow was uniform within a standard deviation of 2.2 %. However, there was a velocity gradient with increasing vertical distance from the floor. The turbulence intensity was also uniform across the plane, within a standard deviation of 0.85 %.

The double random forcing protocol generally produced the highest turbulence intensities, over twice as high as what the oscillations forcing protocol produced. A similar trend with respect to that reported in literature regarding the turbulence intensity versus Rossby number was observed for the double random protocol. The turbulence intensities plateaued relatively early in the Rossby number range. However, the region where the turbulence intensities plateaued was shifted later in the Rossby number range than what was reported by [18]. The oscillations protocol tended to produce relatively constant turbulence intensities, only significantly changing with increasing oscillation amplitude regardless of Rossby number.

The length scales increased linearly with Rossby number for the double random protocol, however, with a steeper slope than what [18] reported. The length scale versus Rossby number for the oscillations case had an even steeper slope, except for the smallest oscillation amplitude of 25° which approximately followed the slope of

the double random mode.

The double random forcing protocol produced flows with high Re_λ and energy spectra with well defined inertial subranges. However, the energy content surpassed that of the on-road measurements made by [8]. The oscillations forcing protocol often produced spectra with large peaks corresponding to the oscillation frequency, a consequence of the forcing protocol being synchronous. In addition, the flows produced by the oscillations mode generally had low Re_λ which greatly diminished the size of the inertial subrange. However, when the oscillations forcing protocol had the vertical shafts operate in double random mode, the produced spectra closely resembled the measured on-road spectra from [8].

6.1 Recommendations

Only limited measurements of the novel TGS system have been presented in this thesis and there remains significant opportunity to further explore the capabilities of the system in the initial designed state.

For example, it was shown that the Rossby number region tested covered mostly moderate and high values beyond those where high variability of the turbulence intensity may be achieved. Therefore, it is recommended to consider these lower values to obtain the lower turbulence intensities even near the grid. Furthermore, measurements in the far field of the current system, would inevitably result in

a range of lower and further homogeneous turbulence. Furthermore, the limited measurements made with the oscillations forcing protocol were shown to extend the range of turbulence that the grid can produce. In one instance, it was shown that a mixed forcing protocol with oscillations and double random may be useful, however, the uniformity of the flow was not assessed in this mode. It was shown that in this mode, the size of the length scales could be greatly increased without appreciably increasing the turbulence intensities and limiting coherent peaks in the spectra.

The current design of the mechanical system elements represents a first test of a new system. Future system development should consider application of reduced blockage grid elements, which are known to lower turbulence intensity while maintaining ability to generate long length scales.

Lastly, as the active grid is only one of three subsystems, and the combined effect of each sub system remains an open topic for further exploration.

A Summary of Results

Table A.1: Summary of the results from the double random protocol.

Test ID	U (m/s)	X/M	$\Omega \pm \omega$ (Hz)	Ro	TI_u (%)	TI_q (%)	u'/v'	L_u (m)	L_u/M	ϵ	λ	Re_λ	C_ϵ
DR1	13.98	10	5±2.5	111.8	33.1	22.63	2.23	0.19	7.6	472	0.0038	1106	0.90
DR1	13.98	20	5±2.5	111.8	24.2	17.08	2.01	0.191	7.64	193	0.0039	859	0.95
DR1	13.98	30	5±2.5	111.8	20.5	15.06	1.8	0.183	7.32	117	0.0045	849	0.91
DR2a	7.08	10	6±3	47.2	29.04	20.48	2.02	0.082	3.28	275	0.0021	255	2.59
DR2a	7.08	20	6±3	47.2	21.77	15.71	1.89	0.091	3.64	94	0.0024	229	2.23
DR2b	14.07	10	6±3	93.8	32.01	22.07	2.17	0.018	0.70	726	0.0032	912	0.14
DR2b	14.07	20	6±3	93.8	22.78	16.35	1.91	0.180	7.18	188	0.0040	854	1.03
DR3	13.92	10	7±3.5	79.5	32.42	22.34	2.17	0.161	6.44	511	0.0033	980	0.90

Test ID	U (m/s)	X/M	$\Omega \pm \omega$ (Hz)	Ro	TI_u (%)	TI_q (%)	u'/v'	L_u (m)	L_u/M	ϵ	λ	Re_λ	C_ϵ
DR3	14.43	20	7±3.5	82.5	23.22	16.67	1.91	0.163	6.52	208	0.0036	805	0.90
DR4a	13.97	10	8±4	69.9	31.89	22.1	2.13	0.15	6	501	0.0034	1005	0.85
DR4a	14.57	20	8±4	72.9	22.69	16.4	1.88	0.153	6.12	199	0.0040	876	0.84
DR4b	14.05	20	8±4	70.3	23.44	16.92	1.88	0.125	5	188	0.0038	836	0.66
DR4b	14.28	30	8±4	71.4	19.15	14.44	1.68	0.128	5.12	138	0.0038	764	0.86
DR5	13.94	10	9±4.5	62.0	31.58	21.95	2.11	0.139	5.56	489	0.0035	1012	0.80
DR5	14.46	20	9±4.5	64.3	22.51	16.32	1.86	0.143	5.72	236	0.0034	730	0.98
DR6a	9.39	10	10±5	37.6	28.65	20.57	1.91	0.091	3.62	239	0.0028	506	1.11
DR6a	9.63	20	10±5	38.5	21.17	15.64	1.77	0.101	4.052	84	0.0036	471	1.00
DR6b	14.14	10	10±5	56.6	31.08	21.72	2.07	0.136	5.46	503	0.0033	950	0.81
DR6b	14.71	20	10±5	58.8	21.99	16.07	1.82	0.138	5.50	203	0.0036	776	0.83
DR7	13.84	10	11±5.5	50.3	30.86	21.64	2.05	0.13	5.06	1017	0.0025	703	1.65
DR7	13.84	20	11±5.5	50.3	21.91	16.07	1.81	0.129	5.16	174	0.0042	879	0.81
DR7	13.84	30	11±5.5	50.3	18.42	14.05	1.64	0.137	5.48	97	0.0043	763	0.80
DR8a	6.72	10	12±6	22.4	23.07	17.84	1.59	0.061	2.44	176	0.0020	209	2.89

Test ID	U (m/s)	X/M	$\Omega \pm \omega$ (Hz)	Ro	TI_u (%)	TI_q (%)	u'/v'	L_u (m)	L_u/M	ϵ	λ	Re_λ	C_ϵ
DR8a	6.69	20	12±6	22.3	18.27	14.22	1.56	0.075	3	54	0.0026	211	2.23
DR8b	13.44	10	12±6	44.8	30.96	21.67	2.06	0.116	4.65	540	0.0030	836	0.87
DR8b	13.44	20	12±6	44.8	21.92	16.03	1.82	0.122	4.88	166	0.0038	767	0.79
DR9	14.03	10	13±6.5	43.2	30.64	21.53	2.04	0.114	4.57	496	0.0033	936	0.71
DR9	14.51	20	13±6.5	44.6	21.74	15.99	1.79	0.120	4.82	192	0.0036	749	0.74
DR15a	9.4	10	14±7	26.9	28.01	20.29	1.87	0.080	3.208	244	0.0027	481	1.07
DR10a	9.59	20	14±7	27.4	20.58	15.38	1.72	0.093	3.712	105	0.0030	442	1.27
DR10b	14.07	10	14±7	40.2	30.49	21.48	2.02	0.112	4.49	408	0.0036	1005	0.58
DR10b	14.6	20	14±7	41.7	21.49	15.84	1.78	0.118	4.728	138	0.0042	862	0.53
DR11	13.6	10	15±7.5	36.3	30.35	21.34	2.04	0.104	4.16	544	0.0029	800	0.80
DR11	14.15	20	15±7.5	37.7	21.59	15.81	1.81	0.114	4.552	170	0.0036	727	0.68
DR12a	9.2	10	16±8	23.0	28.18	20.39	1.87	0.075	2.992	351	0.0025	457	1.51
DR12a	9.41	20	16±8	23.5	20.51	15.34	1.72	0.088	3.536	101	0.0030	412	1.25
DR12b	13.64	10	16±8	34.1	29.43	21.01	1.95	0.106	4.24	794	0.0029	776	1.30
DR12b	14.14	20	16±8	35.4	20.48	15.4	1.7	0.11	4.4	185	0.0036	684	0.84

Table A.2: Summary of the results from the oscillations protocol.

Test ID	U (m/s)	X/M	OA°	OR (Hz)	$\Omega \pm \omega$ (Hz)	TI_u (%)	TI_q (%)	u'/v'	L_u (m)	L_u/M	ϵ	λ	Re_λ	C_ϵ
Open	17.85	10	0	0	-	5.52	4.62	1.40	-	-	66.32	0.0029	126	-
Open	17.89	20	0	0	-	3.31	2.92	1.23	-	-	25.96	0.0017	69	-
OS2	17.89	10	22.5	0.5	-	6.76	5.77	1.30	-	-	92.35	0.0019	154	-
OS2	17.84	20	22.5	0.5	-	4.64	4.00	1.29	-	-	36.74	0.0021	113	-
OS3	17.77	10	22.5	1	-	6.94	5.79	1.36	9.23	369.34	100.27	0.0019	156	493.63
OS3	17.76	20	22.5	1	-	4.84	3.91	1.46	0.96	38.22	36.57	0.0022	125	55.02
OS4	17.74	10	22.5	2	-	7.25	5.95	1.42	0.54	21.55	98.41	0.0020	175	24.92
OS4	17.73	20	22.5	2	-	5.04	4.02	1.51	0.45	18.07	35.06	0.0023	147	22.19
OS5	17.71	10	22.5	4	-	7.24	5.96	1.40	0.26	10.43	100.56	0.0020	173	12.44
OS5	17.7	20	22.5	4	-	5.04	4.08	1.47	0.23	9.22	36.28	0.0022	141	11.77
OS6	17.98	10	22.5	8	-	7.38	6.20	1.35	0.17	6.68	83.55	0.0022	204	5.97
OS6	17.87	20	22.5	8	-	4.97	4.40	1.24	0.15	5.84	29.28	0.0025	149	6.10
OS7	17.93	10	22.5	12	-	7.11	5.91	1.38	0.10	3.84	90.16	0.0021	182	4.18
OS7	17.87	20	22.5	12	-	4.94	4.03	1.44	0.08	3.16	26.98	0.0026	163	3.10

Test ID	U (m/s)	X/M	OA°	OR (Hz)	$\Omega \pm \omega$ (Hz)	TI_u (%)	TI_q (%)	u'/v'	L_u (m)	L_u/M	ϵ	λ	Re_λ	C_ϵ
OS8	17.93	10	22.5	16	-	7.11	5.91	1.38	0.07	2.80	94.31	0.0020	171	3.19
OS8	17.89	20	22.5	16	-	4.97	4.05	1.43	0.07	2.66	29.04	0.0025	155	2.74
OS9	18.07	10	45	0.5	-	9.54	7.61	1.49	-	-	135.56	0.0023	263	-
OS9	18.07	20	45	0.5	-	6.57	5.12	1.57	1.72	68.64	39.88	0.0029	228	40.90
OS10	17.64	10	45	1	-	9.78	7.98	1.44	0.96	38.30	155.86	0.0021	259	29.06
OS10	17.66	20	45	1	-	7.06	5.50	1.60	1.20	48.07	45.75	0.0028	243	28.36
OS11	17.72	10	45	2	-	9.73	7.96	1.43	0.48	19.07	131.64	0.0023	272	12.25
OS11	17.72	20	45	2	-	7.03	5.49	1.59	0.60	23.94	47.94	0.0027	230	14.84
OS12	17.62	30	45	4	-	6.33	4.49	2.04	0.31	12.58	15.60	0.0042	307	3.53
OS12	17.07	20	45	4	-	6.67	4.84	1.97	0.34	13.61	24.10	0.0035	283	5.56
OS12	17.62	10	45	4	-	9.75	7.98	1.44	0.24	9.62	142.20	0.0022	254	6.75
OS12	17.6	20	45	4	-	7.09	5.51	1.61	0.30	12.06	47.18	0.0028	232	7.32
OS13	17.39	10	45	8	-	9.28	8.53	1.15	0.10	4.17	144	0.0020	218	3.57
OS13	17.19	20	45	8	-	5.69	6.10	0.91	0.06	2.54	46.58	0.0022	139	3.16
OS14	17.38	10	45	12	-	9.72	8.04	1.41	0.08	3.28	133.13	0.0023	271	2.26

Test ID	U (m/s)	X/M	OA°	OR (Hz)	$\Omega \pm \omega$ (Hz)	TI_u (%)	TI_q (%)	u'/v'	L_u (m)	L_u/M	ϵ	λ	Re_λ	C_ϵ
OS14	17.36	20	45	12	-	6.93	5.65	1.45	0.09	3.76	48.3	0.0026	211	2.61
OS15	17.59	10	45	16	-	9.54	7.98	1.37	0.06	2.46	133.63	0.0022	249	1.74
OS15	17.53	20	45	16	-	6.60	5.49	1.38	0.07	2.80	46.3	0.0026	200	2.09
OS16	16.98	10	67.5	0.5	-	13.66	10.34	1.72	2.68	107.00	168.79	0.0027	428	36.17
OS16	17.07	20	67.5	0.5	-	9.69	7.18	1.81	2.46	98.26	68.78	0.0031	343	37.33
OS17	17.04	10	67.5	1	-	13.40	10.26	1.67	1.33	53.05	179.33	0.0026	409	19.98
OS17	17.11	20	67.5	1	-	9.34	7.05	1.74	1.21	48.42	67.28	0.003	335	19.95
OS18	17.03	10	67.5	2	-	13.34	10.42	1.65	0.68	27.12	186.11	0.0026	392	10.76
OS18	17.11	20	67.5	2	-	9.30	7.04	1.72	0.62	24.65	67.9	0.0029	312	10.38
OS19	16.36	30	67.5	4	-	8.55	5.97	2.12	0.27	10.92	19.7	0.0048	453	1.97
OS19	16.42	20	67.5	4	-	8.55	6.19	1.94	0.29	11.50	32.16	0.0038	371	3.34
OS19	17.01	20	67.5	4	-	9.64	7.19	1.81	0.31	12.42	64.29	0.0031	350	4.53
OS20	16.64	20	67.5	8	-	6.57	8.92	-	0.05	1.96	55.64	0.0022	161	2.09
OS21	16.44	20	67.5	12	-	7.77	6.28	1.49	0.10	4.04	36.50	0.0032	284	1.77
OS21	16.82	20	67.5	12	-	9.30	7.25	1.60	0.10	3.82	73.27	0.0028	297	1.83

Test ID	U (m/s)	X/M	OA°	OR (Hz)	$\Omega \pm \omega$ (Hz)	TI_u (%)	TI_q (%)	u'/v'	L_u (m)	L_u/M	ϵ	λ	Re_λ	C_ϵ
OS21	16.47	30	67.5	12	-	6.30	5.73	1.18	0.10	4.08	21.99	0.0034	235	2.01
OS22	16.88	20	67.5	16	-	8.72	6.93	1.51	0.07	2.87	69.83	0.0027	263	1.57
OS23	16.79	30	67.5	8	10±5	8.69	6.96	1.47	0.15	5.91	21.25	0.0048	463	1.01
OS23	16.79	20	67.5	8	10±5	9.52	7.33	1.61	0.14	5.65	35.19	0.0041	431	1.22
OS24	16.79	30	67.5	12	10±5	8.16	6.79	1.36	0.14	5.74	21.37	0.0045	408	1.19
OS24	16.79	20	67.5	12	10±5	8.70	7.01	1.45	0.13	5.31	32.25	0.0039	376	1.37
OS25	16.85	30	67.5	16	10±5	8.00	6.70	1.35	0.13	5.28	21.15	0.0045	397	1.14
OS25	16.8	20	67.5	16	10±5	8.60	6.98	1.43	0.12	4.95	31.33	0.0039	375	1.29

B DR7 Turbulence Statistics Example

As was mentioned previously, the data presented for each of the streamwise planes stems from the averaged data from 10 points in the plane. Each of the 10 locations were sampled for 180 s and then the turbulence statistics were calculated for each point before being averaged to give a single value. In this section, an example for the DR7 case is presented.

B.0.1 DR7 Example

For the DR7 case, the mean velocities for the 10 measurement locations are presented in Table B.1 for the 20M plane. The 10 mean flow velocities were then averaged to yield a single mean flow velocity of 14.6 m/s which is the value used when referring to the mean velocity.

Table B.1: Mean velocities for the 10 measurement locations in the 20M plane of DR7.

Mean velocities at each point in the 20M plane (m/s)				
14.31	14.43	14.43	14.52	14.45
14.83	14.76	14.83	14.75	14.71

The turbulence intensity for each measurement point was calculated by taking the RMS of the velocity fluctuations divided by the location's corresponding mean velocity. This process was repeated for each of the 10 measurement locations to give the results presented in Table B.2. All 10 of the calculated turbulence intensity values were then averaged to yield a single turbulence intensity value of 21.9 %, which is the value that is presented in this thesis. This same process was repeated for each of the turbulence statistics (length scale, dissipation rate, isotropy, etc.) presented herein.

Table B.2: Turbulence intensity variation.

Turbulence intensity at each point in the 20M plane (%)				
21.9	21.6	21.5	22.1	22.1
21.7	22.0	22.4	22.0	21.8

C Uncertainty

C.1 x-wire Calibration Error

The majority of the uncertainty realised by x-wire measurements stems from the calibration and from the linearization [70]. Sources of error can stem from the position of the probe, the calculation of the reference velocity, drift in calibrations, and the temperature change between pre- and post-calibrations. Pre- and post-calibrations were done in situ to mitigate potential errors caused by probe position. The probe position error caused by the accuracy of the turntable was so small ($\pm 0.012^{\circ}$) that it can be assumed to be 0.

The total calibration error can be expressed as $\delta_c^2 = \delta_v^2 + \delta_f^2 + \delta_d^2$ where δ_v is the velocity error, δ_f is the fitting error, and δ_d is the calibration drift error. The error associated with the reference velocity δ_v obtained from the pitot probe is dependant on the error from the pressure sensor, δ_p, as well as from the density. The air density error, δ_ρ is dependant on the ambient air temperature error. Ambient temperature variations were minimized through the use of a heat exchanger to maintain the

temperature in the test section to ±1°C. Still, the error associated with the air temperature from the thermocouple is 2 % which corresponds to a density error of $\delta_\rho = 0.11$ % at a temperature of 20°C, as shown below.

At 20°C, a 2 % error corresponds to a temperature error of ±0.4°C. Air pressure was not measured in this research so a constant air pressure of 101.325 kPa is assumed. The specific gas constant, R_{spec}, for air is assumed to be 287. Therefore, the calculation for density and its associated error is as follows.

$$\rho = P_{atm}/R_{spec}T = 101325/287 * (273.15 + (20 \pm 0.4)) = 1.204 \pm 0.002 kg/m^3$$

The error from the pressure sensor is ±1.25 Pa and is taken to be an average from all the calibration velocities. The error for each calibration velocity is given in Table C.1 with the mean error being $\delta_v = 1.1$ %. The drift error, δ_d between the pre- and post-calibrations was $\delta_d = 0.5$ %, however since the calibrations are linearly interpolated and temperature compensated, this value is likely an overly conservative estimate for the drift. The fitting error, δ_f was calculated by averaging the difference between the calibration point measured and the fitted surface for each of the calibration points. The fitting error was calculated to be an average of $\delta_f = 0.05$ %. Since the sources of error are all independent, they can be added quadratically to yield the total calibration error [71] $\delta_c = \sqrt{1.1^2 + 0.05^2 + 0.5^2} = 1.2\%$.

Table C.1: Pressure transducer error for each calibration velocity

Measured Velocity	ΔP	U error (± m/s)	Error (±%)
5	15.1	0.21	4.16
7.3	32.4	0.15	1.93
9.7	56.3	0.12	1.11
12	86.7	0.10	0.72
14.3	123.7	0.09	0.51
16.7	167.2	0.09	0.37
19	217.3	0.08	0.29
21.7	282.6	0.08	0.22
26.7	428.1	0.08	0.15
28.7	495.1	0.08	0.13
			Mean: 1.1

C.2 Double Random Sampling Error - DR7

The uncertainty analysis results are presented here for the DR7 case and are generally representative of the data for the double random forcing protocol as a whole. The sampling error was calculated from $\delta_s = z_\gamma * \sigma/\sqrt{N}$ where z_γ is the z-score associated with the 95 % confidence interval, 1.96, σ is the standard deviation

of the mean velocity, and N is the number of independent samples. An independent sample is taken to be twice the integral time scale τ. For DR7, the integral time scale is $\tau = 9.32e^{-}3$ s. As DR7 was sampled for 180 s, there are N = 180/2*9.32e^{-}3 = 9474 independent samples. If the standard deviation of the flow velocity is $\sigma = 3.18$ m/s, then the margin of error is $MOE = 1.96 * 3.18/\sqrt{9474} = \pm 0.065$ m/s for a 95 % confidence interval. For DR7's mean velocity of 14.6 m/s, the sampling error is $\delta_s = 0.065/14.6 = 0.0045$ or 0.45 %. Since the sampling error and the calibration error are independent, they can be summed quadratically to yield to the total error in the DR7 measurements as $\delta_{tot} = \sqrt{\delta_c^2 + \delta_s^2}$. The total error is $\delta_{tot} = \sqrt{0.012^2 + 0.0045^2} = 1.3$ %.

C.3 Oscillations Sampling Error - OS4 and OS21

The uncertainty analysis results are presented here for the OS4 and OS21 cases and are generally representative of the oscillations cases.

C.3.1 OS4

The sampling error for OS4 was calculated from $\delta_s = z_\gamma * \sigma/\sqrt{N}$ where z_γ is the z-score associated with the 95 % confidence interval, 1.96, σ is the standard deviation of the mean velocity, and N is the number of independent samples. OS4 had $N = 180s/2 * 0.0255s = 3533$ independent samples and a standard deviation

of the velocity of $\sigma = 1.2695$ resulting in a margin of error of $MOE = 1.96 * 1.2695/\sqrt{3533} = \pm 0.042$ m/s for a 95 % confidence interval. For OS4's mean velocity of 17.73 m/s, the sampling error is $\delta_s = 0.042/17.73 = 0.0024$ or 0.24 %. Since the sampling error and the calibration error are independent, they can be summed quadratically to yield to the total error in the OS4 measurements as $\delta_{tot} = \sqrt{\delta_c^2 + \delta_s^2}$. The total error is $\delta_{tot} = \sqrt{0.012^2 + 0.0024^2} = 1.2$ %.

C.3.2 OS21

The sampling error for OS21 was calculated from $\delta_s = z_\gamma * \sigma/\sqrt{N}$ where z_γ is the z-score associated with the 95 % confidence interval, 1.96, σ is the standard deviation of the mean velocity, and N is the number of independent samples. OS21 had $N = 180s/2 * 0.0057s = 15,835$ independent samples and a standard deviation of the velocity of $\sigma = 1.5245$ resulting in a margin of error of $MOE = 1.96 * 1.5245/\sqrt{15,835} = \pm 0.024$ m/s for a 95 % confidence interval. For OS21's mean velocity of 16.82 m/s, the sampling error is $\delta_s = 0.024/16.68 = 0.0014$ or 0.14 %. Since the sampling error and the calibration error are independent, they can be summed quadratically to yield to the total error in the OS21 measurements as $\delta_{tot} = \sqrt{\delta_c^2 + \delta_s^2}$. The total error is $\delta_{tot} = \sqrt{0.012^2 + 0.0014^2} = 1.2$ %.

Bibliography

[1] B. R. McAuliffe, L. Belluz, and M. Belzile. Measurement of the on-road turbulence environment experienced by heavy duty vehicles. *SAE Int. J. Commer. Veh.*, 7:685–702, 09 2014.

[2] K. R. Cooper and S. Watkins. The unsteady wind environment of road vehicles, part one: A review of the on-road turbulent wind environment. In *SAE Technical Paper*. SAE International, 04 2007.

[3] C. Jessing, H. Wilhelmi, F. Wittmeier, A. Wagner, J. Wiedemann, and A. Dillmann. Investigation of transient aerodynamic effects on public roads in comparison to individual driving situations on a test site. Technical report, SAE Technical Paper, 2020.

[4] J. W. Saunders and R. B. Mansour. On-road and wind tunnel turbulence and its measurement using a four-hole dynamic probe ahead of several cars. In *SAE Technical Paper*. SAE International, 03 2000.

[5] J. Saunders and S. Wordley. A review of measurement of ambient turbulence with respect to ground vehicles. In *SAE Technical Paper*, pages 273 – 287. SAE International, 04 2006.

[6] S. Watkins and K. R. Cooper. The unsteady wind environment of road vehicles, part two: Effects on vehicle development and simulation of turbulence. In *SAE Technical Paper*. SAE International, 04 2007.

[7] D. Sims-Williams. Cross winds and transients: Reality, simulation and effects. *SAE Int. J. Passeng. Cars – Mech. Syst.*, 4:172–183, 04 2011.

[8] B. R. McAuliffe, A. Wall, and G. Larose. Simulation of atmospheric turbulence for wind-tunnel tests on full-scale light-duty vehicles. *SAE Int. J. Passeng. Cars - Mech. Syst.*, 9:583–591, 04 2016.

[9] D. Stoll and J. Wiedemann. Active crosswind generation and its effect on the unsteady aerodynamic vehicle properties determined in an open jet wind tunnel. *SAE Int. J. Passeng. Cars - Mech. Syst.*, 11:429–446, 04 2018.

[10] S. Terakado, T. Makihara, T. Sugiyama, K. Maeda, K. Tadakuma, K. Tsuboi, M. Iyota, K. Kosaka, and S. Sugiyama. Experimental investigation of aeroacoustic cabin noise in unsteady flow by means of a new turbulence generating device. *SAE International Journal of Passenger Cars-Mechanical Systems*, 10(2017-01-1545):309–317, 2017.

[11] A. Cogotti. Generation of a controlled level of turbulence in the pininfarina wind tunnel for the measurement of unsteady aerodynamics and aeroacoustics. In *SAE Technical Paper*. SAE International, 03 2003.

[12] O. Mankowski, D. Sims-Williams, and R. Dominy. A wind tunnel simulation facility for on-road transients. *SAE Int. J. Passeng. Cars - Mech. Syst.*, 7:1087–1095, 04 2014.

[13] S. Wordley and J. Saunders. On-road turbulence. *SAE Int. J. Passeng. Cars – Mech. Syst.*, 1:341–360, 04 2008.

[14] S. Wordley and J. Saunders. On-road turbulence: Part 2. *SAE Int. J. Passeng. Cars – Mech. Syst.*, 2:111–137, 04 2009.

[15] L. Mydlarski. A turbulent quarter century of active grids: from makita (1991) to the present. *Fluid Dynamics Research*, 49(6), 12 2017.

[16] J. R. Hearst and B. Ganapathisubramani. Tailoring incoming shear and turbulence profiles for lab-scale wind turbines. *Wind Energy*, 20(12):2021–2035, 2017.

[17] D. Ting. *Basics of Engineering Turbulence*. Elsevier Science, 2016.

[18] J. R. Hearst and P. Lavoie. The effect of active grid initial conditions on high reynolds number turbulence. *Experiments in Fluids*, 56:185, 09 2015.

[19] A. L'Ecuyer. Turbulence generated in a multi-fan wind tunnel. Master's thesis, McGill University, 2022.

[20] M Gordon, R. M. Staebler, J. Liggio, P. Makar, S. Li, J. Wentzell, G. Lu, P. Lee, and J. R. Brook. Measurements of enhanced turbulent mixing near highways. *Journal of Applied Meteorology and Climatology*, 51(9):1618 – 1632, 2012.

[21] S. J. Miller, M. Gordon, R. M. Staebler, and P. A. Taylor. A Study of the Spatial Variation of Vehicle-Induced Turbulence on Highways Using Measurements from a Mobile Platform. *Boundary-Layer Meteorology*, 171(1):1–29, April 2019.

[22] K. S. Rao, R. L. Gunter, J. R. White, and R. P. Hosker. Turbulence and dispersion modeling near highways. *Atmospheric Environment*, 36(27):4337–4346, January 2002.

[23] K. S. Rao, L. Sedefian, and U. H. Czapski. Characteristics of Turbulence and Dispersion of Pollutants Near Major Highways. *Journal of Applied Meteorology*, 18(3):283–293, March 1979.

[24] A. A. Lawson, D. B. Sims-Williams, and R. G. Dominy. Effects of on-road turbulence on vehicle surface pressures in the a-pillar region. *SAE Int. J. Passeng. Cars – Mech. Syst.*, 1:333–340, 04 2008.

[25] A. A. Lawson, R. G. Dominy, D. B. Sims-Williams, and P. Mears. A comparison between on-road and wind tunnel surface pressure measurements on a mid-sized hatchback. In *SAE Technical Paper*, volume 116, pages 983–992. SAE International, 04 2007.

[26] N. Oettle, D. Sims-Williams, R. Dominy, C. Darlington, C. Freeman, and P. Tindall. The effects of unsteady on-road flow conditions on cabin noise. In *SAE Technical Paper*, volume 4, pages 120–130. SAE International, 04 2010.

[27] B. R. McAuliffe and A. D'Auteuil. A system for simulating road-representative atmospheric turbulence for ground vehicles in a large wind tunnel. *SAE International Journal of Passenger Cars-Mechanical Systems*, 9(2016-01-1624):817–830, 2016.

[28] H. Wilhelmi, C. Jessing, J. Bell, D. Heine, A. Wagner, J. Wiedemann, and C. Wagner. Simulation of transient on-road conditions in a closed test section wind tunnel using a wing system with active flaps. In *SAE Technical Paper*. SAE International, 04 2020.

[29] R. Blumrich, N. Widdecke, J. Wiedemann, A. Michelbach, F. Wittmeier, and O. Beland. New fkfs technology at the full-scale aeroacoustic wind tunnel of university of stuttgart. *SAE International Journal of Passenger Cars-Mechanical Systems*, 8(2015-01-1557):294–305, 2015.

[30] T. Yamashita, T. Makihara, K. Maeda, and K. Tadakuma. Unsteady aerodynamic response of a vehicle by natural wind generator of a full-scale wind

tunnel. *SAE International Journal of Passenger Cars-Mechanical Systems*, 10(2017-01-1549):358–368, 2017.

[31] G. Larose, A. Wall, B. R. McAuliffe, D. Kelly, G. K. Stone, and W. N. Yakymyk. Sectional model investigation at high reynolds number for a super tall building. *Journal of Wind Engineering and Industrial Aerodynamics*, 104:49–55, 2012.

[32] R. Lee, B. McAullife, and G. Larose. Wind-tunnel investigation of a large scale pressure model of the shanghai centre, shanghai, china. Technical report ltr-al-2009-0004, National Research Council Canada, 2010.

[33] G.L. Larose, A. Wall, B.R. McAuliffe, D. Kelly, G. Stone, and W. Yakymyk. Sectional model investigation at high reynolds number for a super tall building. *Journal of Wind Engineering and Industrial Aerodynamics*, 104-106:49–55, 2012. 13th International Conference on Wind Engineering.

[34] C. S. Shet, M. R. Cholemari, and S. V. Veeravalli. Optimizing the performance of an active grid to generate high intensity isotropic free stream turbulence. *Physics of Fluids*, 32(9):095120, 2020.

[35] E. Bodenschatz, G. P. Bewley, H. Nobach, M. Sinhuber, and H. Xu. Variable density turbulence tunnel facility. *Review of Scientific Instruments*, 85(9), 2014.

[36] E. Muñiz Pladellorens and P. Riera Turró. *Generation of atmospheric turbulence in a wind tunnel*. PhD thesis, UPC, Escola d'Enginyeria de Barcelona Est, Oct 2017.

[37] M. Hideharu. Realization of a large-scale turbulence field in a small wind tunnel. *Fluid Dynamics Research*, 8(1):53–64, 1991.

[38] S. C. Ling and C. A. Wan. Decay of isotropic turbulence generated by a mechanically agitated grid. *Physics of Fluids*, 15(8):1363–1369, August 1972.

[39] R. Vonlanthen and P. Monkewitz. A novel tethered-sphere add-on to enhance grid turbulence. *Experiments in Fluids*, 51:579–585, 09 2011.

[40] A. Danesh-Yazdi, O. Goushcha, N. Elvin, and Y. Andreopoulos. Fluidic energy harvesting beams in grid turbulence. *Experiments in Fluids*, 56:161, 08 2015.

[41] L. Neuhaus, F. Berger, J. Peinke, and M. Hölling. Exploring the capabilities of active grids. *Experiments in Fluids*, 62:1–12, 06 2021.

[42] H. Makita and K. Sassa. Active turbulence generation in a laboratory wind tunnel. In *Advances in Turbulence 3*, pages 497 – 505, Berlin, Heidelberg, 1991. Springer Berlin Heidelberg.

[43] H. Makita and K. Sassa. Active turbulence generation in a laboratory wind tunnel. In Arne V. Johansson and P. Henrik Alfredsson, editors, *Advances in Turbulence 3*, pages 497–505, Berlin, Heidelberg, 1991. Springer Berlin Heidelberg.

[44] X. Shenand and Z. Warhaft. The anisotropy of the small scale structure in high reynolds number turbulent shear flow. *Physics of Fluids*, 12(11):2976–2989, 2000.

[45] J. V. Larssen and W. J. Devenport. On the generation of large-scale homogeneous turbulence. *Experiments in Fluids*, 50(5):1207–1223, 05 2011.

[46] P. Knebel, A. Kittel, and J. Peinke. Atmospheric wind field conditions generated by active grids. *Experiments in Fluids*, 51:471–481, 08 2011.

[47] L. Mydlarski and Z. Warhaft. On the onset of high reynolds number grid-generated wind tunnel turbulence. *Journal of Fluid Mechanics*, 320:331–368, 08 1996.

[48] L. Mydlarski and Z. Warhaft. Passive scalar statistics in high-péclet-number grid turbulence. *Journal of Fluid Mechanics*, 358:135–175, 03 1998.

[49] R. E. G. Poorte and A. Biesheuvel. Experiments on the motion of gas bubbles in turbulence generated by an active grid. *Journal of Fluid Mechanics*, 461:127 – 154, 06 2002.

[50] K. P. Griffin, N. J. Wei, E. Bodenschatz, and G. P. Bewley. Control of long-range correlations in turbulence. *Experiments in Fluids*, 60(4), mar 2019.

[51] H. E. Cekli, R. Joosten, and W. van de Water. Stirring turbulence with turbulence. *Physics of Fluids*, 27(12):125107, 2015.

[52] A. Thormann and C. Meneveau. Decay of homogeneous, nearly isotropic turbulence behind active fractal grids. *Physics of Fluids*, 26:025112, 01 2014.

[53] H. S. Kang, S. Chester, and C. Meneveau. Decaying turbulence in an active-grid-generated flow and comparisons with large-eddy simulation. *Journal of Fluid Mechanics*, 480:129–160, 2003.

[54] H. Cekli and W. Water. Tailoring turbulence with an active grid. *Experiments in Fluids*, 49:409–416, 08 2010.

[55] J. R. Hearst and B. Ganapathisubramani. Tailoring incoming shear and turbulence profiles for lab-scale wind turbines. *Wind Energy*, 20:2021–2035, 08 2017.

[56] N. Reinke, T. Homeyer, M. Hölling, and J. Peinke. Flow modulation by an active grid. page arXiv:1703.00721, 03 2017.

[57] L. Kröger, J. Frederik, J. W. Wingerden, J. Peinke, and M. Hölling. Generation of user defined turbulent inflow conditions by an active grid for validation experiments. *Journal of Physics: Conference Series*, 1037:052002, 06 2018.

[58] L. Neuhaus, M. Hölling, W. Bos, and J. Peinke. Generation of atmospheric turbulence with unprecedentedly large reynolds number in a wind tunnel. *Physical Review Letters*, 125:154503, 10 2020.

[59] M. Herbert, T. Skeledzic, H. Lienhart, and Özgür Ertunc. Effect of the motion pattern on the turbulence generated by an active grid. In A. Dillmann, G. Heller, E. Krämer, and C. Wagner, editors, *New Results in Numerical and Experimental Fluid Mechanics XIII*, pages 37–46. Springer International Publishing, 2021.

[60] R. Lueptow, K. Breuer, and J. Haritonidis. Computer-aided calibration of x-probes using a look-up table. *Experiments in Fluids*, 6:115–118, 01 2004.

[61] G Comte-Bellot. Hot-wire anemometry. *Annual Review of Fluid Mechanics*, 8(1):209–231, 1976.

[62] P. Burattini and R. A. Antonia. The effect of different x-wire calibration schemes on some turbulence statistics. *Experiments in Fluids*, 38:80–89, 12 2005.

[63] A. J. Puga and J. C. LaRue. Normalized dissipation rate in a moderate taylor reynolds number flow. *Journal of Fluid Mechanics*, 818:184–204, 2017.

[64] G. Vita, H. Hemida, T. Andrianne, and C. C. Baniotopoulos. Generating atmospheric turbulence using passive grids in an expansion test section of a wind tunnel. *Journal of Wind Engineering and Industrial Aerodynamics*, 178:91–104, 2018.

[65] S. B. Pope. *Turbulent Flows*. Cambridge University Press, 2000.

[66] Henk Tennekes and John L. Lumley. *A First Course in Turbulence*. The MIT Press, 03 1972.

[67] D. O. Mora, E. Muñiz Pladellorens, P. Riera Turró, M. Lagauzere, and M. Obligado. Energy cascades in active-grid-generated turbulent flows. *Phys. Rev. Fluids*, 4:104601, Oct 2019.

[68] J. Christos Vassilicos. Dissipation in turbulent flows. *Annual Review of Fluid Mechanics*, 47(1):95–114, 2015.

[69] W. J. T. Bos, L. Shao, and J.-P. Bertoglio. Spectral imbalance and the normalized dissipation rate of turbulence. *Physics of Fluids*, 19(4):045101, 2007.

[70] Finn Jørgensen. How to measure turbulence with hot-wire anemometers - a practical guide. 2002.

[71] J.R. Taylor. *An Introduction to Error Analysis: The Study of Uncertainties in Physical Measurements*. ASMSU/Spartans.4.Spartans Textbook. University Science Books, 1997.